



## Diplomarbeit

# Physically based modelling of a high-speed pantograph

ausgeführt zum Zwecke der Erlangung des akademischen Grades eines Diplom-Ingenieurs  
unter der Leitung von

Ao.Univ.Prof. Dipl.-Ing. Dr.techn. Martin Kozek  
und

Univ.Ass. Dipl.-Ing. Dr.techn. Alexander Schirrer  
Institut für Mechanik und Mechatronik  
E325 A5

eingereicht an der Technischen Universität Wien

**Fakultät für Maschinenwesen und Betriebswissenschaften**

von

Guilherme Aschauer  
Matr.Nr.: 0627911  
Rallenweg 18  
1220 Wien

Wien, am 25. November 2014

---

Guilherme Aschauer

## Eidesstattliche Erklärung

Ich erkläre eidesstattlich, dass ich die Arbeit selbständig angefertigt, keine anderen als die angegebenen Hilfsmittel benutzt und alle aus ungedruckten Quellen, gedruckter Literatur oder aus dem Internet im Wortlaut oder im wesentlichen Inhalt übernommenen Formulierungen und Konzepte gemäß den Richtlinien wissenschaftlicher Arbeiten zitiert, durch Fußnoten gekennzeichnet bzw. mit genauer Quellenangabe kenntlich gemacht habe.

Wien, am 25. November 2014

---

Guilherme Aschauer

## Kurzfassung

Stromabnehmer moderner Hochgeschwindigkeitszüge stellen im Moment den limitierenden Faktor im Bestreben nach Erreichen immer höherer Geschwindigkeiten dar. Ihre Aufgabe ist es, den permanenten Kontakt zwischen Zug und der stromführenden Oberleitung zu gewährleisten, dabei jedoch die entstandene Kontaktkraft so gering wie möglich zu halten, da dies sonst zu starken und schnellen Abnutzungserscheinungen an allen involvierten Bauteilen führen kann. Aus diesen Gründen kommt der Pantographenentwicklung in jüngerer Vergangenheit eine immer stärker werdende Rolle zu.

Ziel dieser Arbeit ist die Herleitung eines Pantographenmodells mit physikalisch interpretierbaren Parametern. Dies ermöglicht einerseits Variantenstudien und trägt andererseits zur besseren Interpretierbarkeit des Modells bei. Darüberhinaus war die Anbindung an den bereits vorhandenen Pantographenprüfstand und die Messdatenerfassung ebenfalls Teil dieser Arbeit. Außerdem wurden Videoaufzeichnungen von den Prüfstandsläufen aufgenommen, aus denen anschließende Positionsinformationen von verschiedenen Pantographenteilen extrahiert wurde. Die Messdaten wurden anschließend zur Parameteridentifikation herangezogen, und das erhaltene (nichtlineare) Modell linearisiert und mit anderen, in der Literatur gebräuchlichen Modellstrukturen verglichen.

Abschließend wurde das Thema *Design of Experiment* besprochen, das dazu dient, die einzelnen Modellparameter mit möglichst geringer Unsicherheit zu schätzen.

## Abstract

Pantographs are the connecting element between the train and the current-carrying contact wire and are so far the limiting factor in the attempt of reaching higher speeds in the railway industry. Their task is to establish a reliable permanent connection between the train and the contact wire while keeping the needed contact force as low as possible to minimise the wear of each element. Hence, scientific research has increasingly focused on pantographs in the last years.

The aim of this work is to obtain a model of a pantograph with physical interpretable parameters. This approach allows to study the influence of each parameter on the performance of the pantograph and furthermore leads to interpretable model states. Additionally, the testbed connection as well as the measurement data acquisition was also part of this work. Moreover, video recordings of each test run were made from which the position of different pantograph parts could be extracted. The so obtained measurement data was then used in the parameter estimation process. The obtained nonlinear model was linearised and compared to other model structures appearing in the literature.

Finally, the topic of *Design of Experiment* is introduced, allowing to estimate the model parameters as accurately as possible.



# Contents

<b>1</b>	<b>Introduction</b>	<b>1</b>
<b>2</b>	<b>Modelling</b>	<b>5</b>
2.1	Kinematics . . . . .	5
2.1.1	Angular Formulation . . . . .	5
2.1.2	Velocity Formulation . . . . .	9
2.2	Collector-Head . . . . .	10
2.3	Equations of Motion . . . . .	10
2.4	Linearisation . . . . .	12
2.5	Extensions to the Model . . . . .	13
2.6	Simple Model Structures . . . . .	14
2.7	Friction . . . . .	15
<b>3</b>	<b>Test Bed and Measurement Interface</b>	<b>17</b>
3.1	MicroAutoBox II Interface . . . . .	18
3.2	Video Position Measurement and Synchronisation . . . . .	21
3.3	Extracting Position Measurement from Camera Recording . . . . .	25
3.3.1	Conversion Process . . . . .	25
3.3.2	Comparison of Different Sensors . . . . .	28
<b>4</b>	<b>Identification Process</b>	<b>30</b>
4.1	Theoretical Background . . . . .	30
4.1.1	Gradient-Based optimisation . . . . .	31
4.1.2	Genetic Algorithm . . . . .	33
4.1.3	Methodology – Implementation of the Parameter Estimation . . . . .	34
4.2	Measurement Data . . . . .	35
4.3	Collector-Head . . . . .	38
4.4	Nonlinear Pantograph Model with Force Excitation . . . . .	41
4.5	Nonlinear Pantograph Model with Displacement Excitation . . . . .	41
4.6	Harmonic Oscillators . . . . .	44
4.7	Harmonic Oscillators with Friction . . . . .	44
4.8	Summary . . . . .	45
<b>5</b>	<b>Design of Experiment — DoE</b>	<b>47</b>
5.1	Introduction . . . . .	47

---

5.2	Theory . . . . .	47
5.3	Example: Slope and Intercept of a Line . . . . .	49
5.4	Example: Dynamical System . . . . .	50
5.5	Application to Pantograph Testbed . . . . .	56
<b>6</b>	<b>Summary/Outlook</b>	<b>58</b>
	<b>Bibliography</b>	<b>60</b>

# List of Figures

1.1	System of the catenary/pantograph interaction, taken from [1] . . . .	1
2.1	Pantograph . . . . .	6
2.2	The four bar substitute linkage for the arrangement of rods. Dimen- sions in Table 2.1 . . . . .	6
2.3	The four bar linkage from Figure 2.2 with an additional degree of freedom and an attached bar with the length $l_4$ . . . . .	8
2.4	Trajectory of the cross bar when $\varphi_1$ is varied . . . . .	9
2.5	Substituted mechanical system of the collector-head (pan-heads and torsion springs) which is mounted on the cross bar . . . . .	10
2.6	The main pantograph model used . . . . .	11
2.7	Illustration of the state space system (2.29) as a block diagram. . . .	13
2.8	An extended pantograph model where the carbon contact is modelled as a spring . . . . .	14
2.9	Two-mass-oscillator . . . . .	15
2.10	Two friction models . . . . .	16
3.1	Schematic drawing of the pantograph testbed, taken from [2] 18	
3.2	Signals processed by the MicroAutoBox II (left: Sensors, right: actu- ators) . . . . .	18
3.3	Screenshot of the developed ControlDesk GUI . . . . .	19
3.4	Contact wire deflection (two periods from a simulation) of a simu- lated catenary/pantograph interaction (train speed 300 km/h, passive pantograph). . . . .	20
3.5	Illustration of the signal processing before the position demand com- mand is sent to the linear motor. . . . .	20
3.6	Logics used to limit the maximum position error per sample for the linear motor . . . . .	21
3.7	An extract of the LED synchronisation signal sent by the MABX (blue) and two slower sampled camera measurements (green and red) starting at slightly different instants of time that lead to exactly the same sequence . . . . .	23

3.8	Results of the correlation analysis. The value of 1 (perfect correlation) was not reached because 10 % of the camera bits were artificially flipped. The left plot shows the result of the cross-correlation between the downsampled MABX LED sequence and the camera recording. The right plot shows that it does matter which of the ten first fine data points is the starting sample of the downsampling. . . . .	24
3.9	Setting up a region inside which the marker is expected to remain . .	26
3.10	Steps of the marker detection process . . . . .	27
3.11	Extracted measurement of the cross-bar position and the signals of the two laser sensors. . . . .	29
3.12	Linear motor's slider position received via CAN-bus (gray) and the extracted position signal from the video recordings (black). . . . .	29
4.1	Spectrum of the force signal with two different sampling frequencies when the linear motor is excited with a 1 Hz sine. . . . .	36
4.2	Recorded values for two distinct APRBS input sequences (linear motor's position and pressure) . . . . .	37
4.3	Recorded values for two distinct ramp input sequences (linear motor's position and pressure). During the first 60 s the linear motor is moving and although already low-pass filtered, the oscillations of the force signal are clearly visible. . . . .	37
4.4	Measured position (gray) and estimated (black) transfer function from the cross-bars position to the pan-heads position. . . . .	39
4.5	Measured (gray) and estimated (black) transfer functions from the cross-bars position and the force to the pan-heads relative position. .	40
4.6	Measured (gray) and estimated (black) transfer functions from the force $F_1$ to $\Delta Y = y_{cb} - y_h$ . . . . .	40
4.7	Pareto front of the identification process to the nonlinear pantograph model . . . . .	42
4.8	Force signal from the validation runs . . . . .	43
4.9	Eigenvalues of the linearised system when each of the parameters is multiplied by 0.9 (circles) and 1.1 (crosses), respectively . . . . .	43
4.10	Force signal measured (black, thin) and the model output of the harmonic oscillators: 2-mass-model: gray, 3-mass-model: black, thick . .	44
5.1	Result of the DoE for obtaining the slope and intercept of a line with two measurements (red dots). . . . .	50
5.2	One degree of freedom oscillator . . . . .	51
5.3	Input (force, dashed) and corresponding system response (position, gray) obtained with the sine wave force signal. . . . .	54
5.4	Input (force, dashed) and corresponding system response (position, gray) obtained with the force signal from the offline DoE. . . . .	55
5.5	Input (force, dashed) and corresponding system response (position, gray) obtained with the force signal from the online DoE. . . . .	55

# Chapter 1

## Introduction

Pantographs are the overhead systems mounted on electrical trains which should guarantee a permanent contact between the train and the current-carrying contact wire. In former times, electrical trains stood in competition with several other types of driving systems but nowadays steam locomotives as well as trains powered by internal combustion engines have nearly vanished, while the average driving speed of high-speed trains has increased dramatically. This led to new problems and demands on the train and the attached pantograph.

At high speeds (above 250 km/h), even small disturbances in the overhead line or even the normal irregularities caused by the droppers hanging from the messenger wire holding the contact wire can have a significant impact on the pantograph and may lead to contact loss which should be avoided. Figure 1.1 schematically depicts the pantograph/catenary interaction.

The loss of contact of the pantograph not only causes a drop in electrical power provided to drive the train, it also poses a great problem in means of wear on the contact wire and the pantograph, as the resulting effects ('electric arc') are analogous to arc welding [3]. While the design of the pantograph already partly incorporates the harsh environment in which the parts are operating, and therefore permits a relatively easy replacement of the carbon collector strips, the repair of the catenary system requires much more effort. Since this means a complete opening of circuit, the route is completely out of order for the maintenance time.

One approach to avoid this undesired loss of contact would be to increase the force

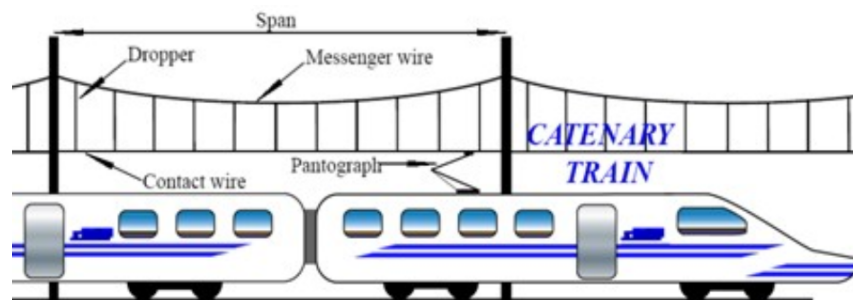


Figure 1.1: System of the catenary/pantograph interaction, taken from [1]

with which the collector-carrying pan-head is pressed against the contact wire by raising the pressure inside the pneumatic actuator at the bottom of the pantograph that generates the uplift force. This, of course, would guarantee a better contact in most cases but, in turn, leads to a greater mechanical wear due to increased friction and also to larger displacements of the catenary. In addition, the dynamics of the pantograph/catenary interaction are altered by an unintended high force pressing against the contact wire. Furthermore, there are standardised nominal forces depending on the speed of the train. Some manufacturers circumvent this by appropriately placing wings on the pantograph, automatically increasing the uplift force at higher speeds by aerodynamic effects. This approach needs special empirical adjustment for every single pantograph during test drives and cannot be easily accomplished in the production halls. Furthermore, the whole pantograph and especially the wing foils are exposed to environmental influences like hitting objects and icing, which may lead to altered dynamics and unintended behaviour.

Since the international trend in high-speed rail traffic goes towards increasing speeds, these problems become more pressing. The limiting factors on speed are geometrical and topological conditions, the drag (proportional to the square of the velocity), as well as noise and the already described problems of maintaining a steady contact between the pantograph and the contact wire. One approach to reduce the influence of the latter are actively controlled pantographs. However, some barriers have to be taken for them to work. High currents flow through the pantograph in order to power the engines and the on-board equipment. However, this high-current environment is not suitable for microcontrollers and other electronic devices like actuators and sensors that are needed for a high-performance active control of pantographs. Furthermore, the power source for these devices, if not directly driven by the train supply current, is critical because there is no connection for such devices planned or possible on common trains.

One solution would be to use the pneumatic actuator at the bottom of the pantograph as an actuator for active control [4]. However, its bandwidth is strongly limited and the time delays introduced by this approach are significant as the logic can only be implemented at the front of the wagon where the compressed air supplying device is attached. Additionally, there is a delay in the response of the bellow to a change in the height of the pan-head through a change in the contact wire level as well. A different approach is to utilise the incident air arising at high speed travel as a power source to actively control the angle of attack of attached airfoils [5].

Furthermore, in order to control the pantograph, a mathematical model of the pantograph is needed. While some papers on concepts of placing additional actuator devices to dynamically control the pantograph were already published in the early nineties [6], the underlying models are widely made up of lumped parameter models of a translational mass/spring/damper-system.

Although some attempts to scientifically investigate the behaviour of the pantograph and its interaction with a contact wire were already made in the 1960s, the modelling approach has only slowly changed over the years. For example, in 1966 Gilbert and Davies [7] already investigated a pantograph's motion on a nearly uniform overhead

line by modelling it as a simple two-mass system where the first mass is only supported to the frame by a damper but no spring. The same pantograph model was used five years later by Ockendon and Tayler [8] to investigate the dynamics of the pantograph/wire interaction while considering the changing stiffness of the system by the placement of droppers. A more sophisticated pantograph modelling approach was finally taken in [9], where a nonlinear pantograph model was derived and analysed. However, as will be shown later in Chapter 2, not even the kinematics of the pantograph are described satisfactorily by this model.

In the past, pantograph models mainly appeared in the literature when investigating the pantograph/catenary interaction and while the latter was described by increasingly involved coupled PDEs, the pantograph models are often still represented as translational linear systems consisting of springs, masses and dampers [10, 11, 12]. Sometimes, the pantograph's head is connected on a rotary joint to the linkage [13, 14, 15], in order to represent the rotation that the two pan-heads can undergo when, for example, the contact wire changes its height. However, in the last few years the dynamics of the pantograph have been investigated in more detail. For example, even a 9 degree of freedom model is described in [16], but it is still made up of translational oscillators. Later, multi-body models based on the real physics were proposed [17]. There, the pantograph-catenary interaction was investigated and a framework for using two different solvers (one for the catenary with finite difference models and one for the pantograph with variable time step size) with appropriate coupling was introduced. A multibody model created in SIMPACK and analyzed by a finite element method was described in [16]. In [18], a multibody model of the pantograph was used to investigate the influence of the aerodynamical forces on the pantograph during high-speed travel. In [19], the nonlinear behaviour of a special current collector suspension (the collector-head on top of the arrangement of rods) made out of two springs that introduce nonlinearities because of their special alignment was investigated. A more detailed overview over different pantograph models can be found in [20].

In this work an interpretable, physically based pantograph model is derived. Before that a connection to the already existing pantograph testbed is established and test runs are made. The unknown parameters of the model are then estimated and the resulting model is compared to generic model structures. The main contributions of this work can be summarised as:

**Pantograph modelling** : A modular, physically based multibody model of a pantograph is formulated, which captures the relevant physical effects as accurate as possible while keeping the complexity at a reasonably low level. With the derived model, parameter studies should be possible, which a priori rules out black-box models. The designated application of the resulting model lies in the development of pantographs in the coupled pantograph/catenary simulation environment. The results of the modelling process are described in Chapter 2.

**Testbed connection** : A reliable testbed connection for data acquisition is established and an easy-to-use testbed interface is developed that allows to control the actuators.

**Measurement signal synchronization** : Coloured labels were attached to the pantograph and video recordings of the test runs were made. Position information of the labels were extracted and had to be synchronised correctly to the other measurements having a much higher sampling rate. The methodology of obtaining sensor data and joining the measurements obtained from the testbed and the position information extracted from video recordings is described in Chapter 3.

**Physical parameter estimation** : Because only information on the length of the different pantograph parts is available and no reliable data about masses and spring constants could be retrieved, identification runs had to be made to estimate these model parameters, which is described in Chapter 4.

**Model evaluation and comparison** : The developed model that is based on physical principles is compared to various other model structures that can be found in the literature, whose parameters are estimated for the studied pantograph as well. In Chapter 4, all model structures are compared in terms of quality (fit) and physical interpretability.

**Outlook to design-of-experiment methods** : The basic design-of-experiment (DoE) methods are outlined that are necessary to generate optimal measurement plans for the identification tasks. The goal is to obtain as much information as possible from a future or even ongoing experiment. Examples of model-based DoE methods for simple model structures are shown, and the future application for the pantograph model is sketched.



# Chapter 2

## Modelling

The typical layout of a standard pantograph of the company Siemens (formerly MELECS) is depicted in Figure 2.1. This layout served as the basis of the modelling process. The heaviest part is the frame on which the lower arm (both made of steel) is attached. The slim thrust rod is only tension loaded and has therefore much smaller dimensions. Although the upper arm is the largest component, its mass is about the same as the lower arm's mass because it is made out of aluminium. The two ends of the upper arm are connected by the cross bar. The pan heads are mounted on top of the cross bar via torsional springs. The raising torque is applied by a pneumatic actuator between the frame and the lower arm. This pneumatic actuator can be driven with up to 10 bar that are provided at the front of each train the pantograph is mounted on. Due to the long distance and the inertia of the pneumatic system, the actual actuator bandwidth is strongly limited and imposes an upper limit on the possible control dynamics. This could be circumvented by placing additional actuators (and sensors) closer to the pan heads that try to maintain contact with the catenary wire and additionally reduce the force needed. However, so far only ideas and early, conceptual prototypes exist [21, 22, 4]. In practice, the small scale and high frequency disturbances are rejected or absorbed passively via the collector head suspension only.

### 2.1 Kinematics

In this section the kinematic equations of the pantograph are derived. First, only the static connection between the various elements is described, before the derivations of these quantities with respect to time are introduced. This finally enables the derivation of the equations of motion.

#### 2.1.1 Angular Formulation

Only the small-scale motion of the pantograph is done by the torsion spring on top of the upper arm, while large displacements are accomplished through the arrangement of the rods. To describe their kinematics, the substituted mechanical system depicted in Figure 2.2 is investigated. The dimensions of the individual parts of the test

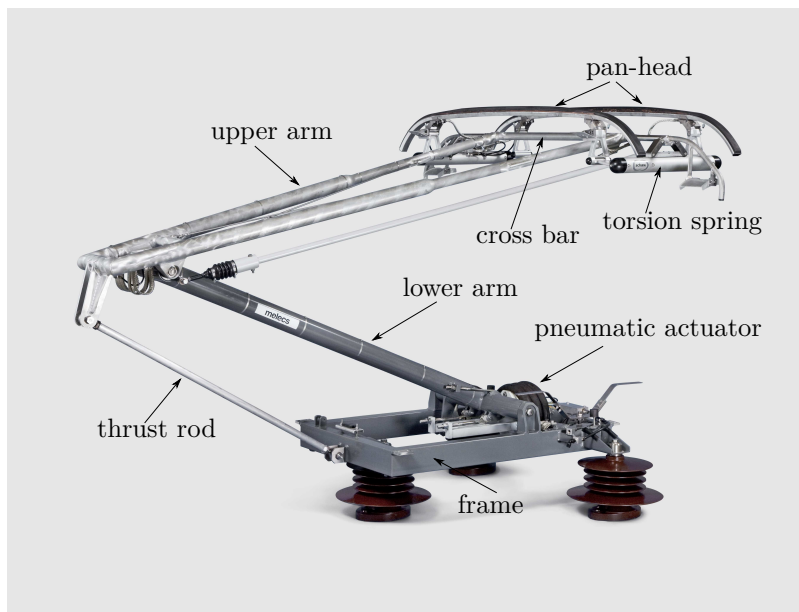


Figure 2.1: Pantograph

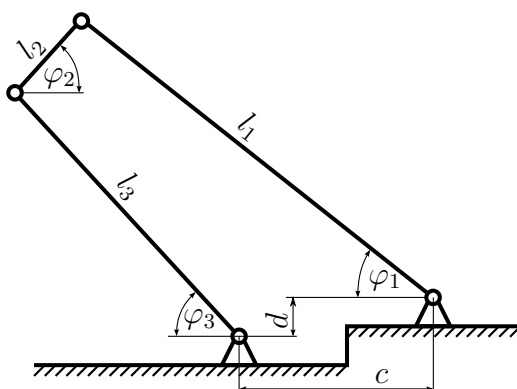


Figure 2.2: The four bar substitute linkage for the arrangement of rods. Dimensions in Table 2.1

quantity	length in m
$l_1$	1.600
$l_2$	0.314
$l_3$	1.182
$l_4$	1.910
$c$	0.720
$d$	0.150

Table 2.1: Dimensions of the test pantograph

pantograph can be found in Table 2.1.

First, the geometric relations are formulated by summing up the horizontal and vertical lengths to two equations:

$$l_1 \cos(\varphi_1) + l_2 \cos(\varphi_2) = c + l_3 \cos(\varphi_3), \quad (2.1)$$

$$l_2 \sin(\varphi_2) + l_3 \sin(\varphi_3) = d + l_1 \sin(\varphi_1). \quad (2.2)$$

Then, by rearranging by putting the terms with  $l_3$  and  $\varphi_3$  on one side, squaring both equations and eventually adding them, one gets after some simplifications:

$$\underbrace{l_3^2 \cos^2(\varphi_2) + \sin^2(\varphi_2)}_{=1} = l_1^2 + l_2^2 + c^2 + d^2 + 2dl_1 \sin \varphi_1 - 2cl_1 \cos \varphi_1 + 2l_2(l_1 \cos \varphi_1 - c) \cos \varphi_2 - 2l_2(l_1 \sin \varphi_1 + d) \sin \varphi_2$$

This finally leads to the following equation:

$$k_1(\varphi_1) \sin(\varphi_2) + k_2(\varphi_1) \cos(\varphi_2) + k_3(\varphi_1) = 0, \quad (2.3)$$

where  $k_i$  are functions of the arbitrarily chosen independent variable  $\varphi_1$ :

$$k_1(\varphi_1) = -2l_2(l_1 \sin \varphi_1 + d), \quad (2.4)$$

$$k_2(\varphi_1) = 2l_2(l_1 \cos \varphi_1 - c), \quad (2.5)$$

$$k_3(\varphi_1) = l_1^2 + l_2^2 - l_3^2 + c^2 + d^2 + 2dl_1 \sin \varphi_1 - 2cl_1 \cos \varphi_1. \quad (2.6)$$

Equation (2.3) is sometimes referred to as *Freudenstein Equation* and can be analytically solved in closed form by defining:

$$t = \tan \frac{\varphi_2}{2} \quad (2.7)$$

from which directly follows:

$$\cos \varphi_2 = \frac{1 - t^2}{1 + t^2} \quad (2.8)$$

$$\sin \varphi_2 = \frac{2t}{1 + t^2}. \quad (2.9)$$

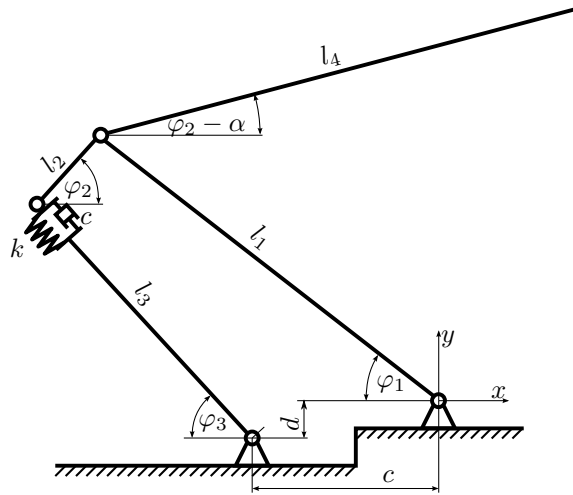


Figure 2.3: The four bar linkage from Figure 2.2 with an additional degree of freedom and an attached bar with the length  $l_4$ .

By substituting in (2.3) the following quadratic equation is derived:

$$t^2(k_3 - k_2) + t(2k_1) + (k_2 + k_3) = 0 \quad (2.10)$$

which eventually gives a solution for  $\varphi_2(\varphi_1)$ :

$$\varphi_2(\varphi_1) = 2 \arctan \frac{-k_1 \pm \sqrt{k_1^2 + k_2^2 - k_3^2}}{k_3 - k_2}. \quad (2.11)$$

By using this result, as well as equations (2.1) and (2.2),  $\varphi_3(\varphi_1, \varphi_2)$  can be calculated, where  $\varphi_2$  could be eliminated by using equation (2.11):

$$\varphi_3(\varphi_1, \varphi_2) = \arctan \frac{l_1 \sin \varphi_1 - l_2 \sin \varphi_2 + d}{l_1 \cos \varphi_1 + l_2 \cos \varphi_2 - c}. \quad (2.12)$$

Attaching another bar with the length  $l_4$  in a fixed angle  $\alpha$  to the second bar, as shown in Figure 2.3, the position of the cross bar can be described by the knowledge of just one angle if all bars are considered rigid:

$$x_{\text{crossbar}} = -l_1 \cos(\varphi_1) + l_4 \cos(\varphi_2 - \alpha), \quad (2.13)$$

$$y_{\text{crossbar}} = l_1 \sin(\varphi_1) + l_4 \sin(\varphi_2 - \alpha). \quad (2.14)$$

The trajectory that the cross bar undergoes with varying  $\varphi_1$  is depicted in Figure 2.4. It is in perfect agreement with the CAD-data provided by the manufacturer.

As can be seen, the horizontal position of the cross bar is varying dependent on the angle  $\varphi_1$  and indicates the strong nonlinearities inside the system.

It turns out that the arrangement of rods shows flexible behaviour, which is probably due to the light weight construction of the bars and elasticities and imperfections of the hinges and bushings. It is assumed that those effects can be modelled by linear springs. Mainly the upper arm shows some flexible beam behaviour and the other

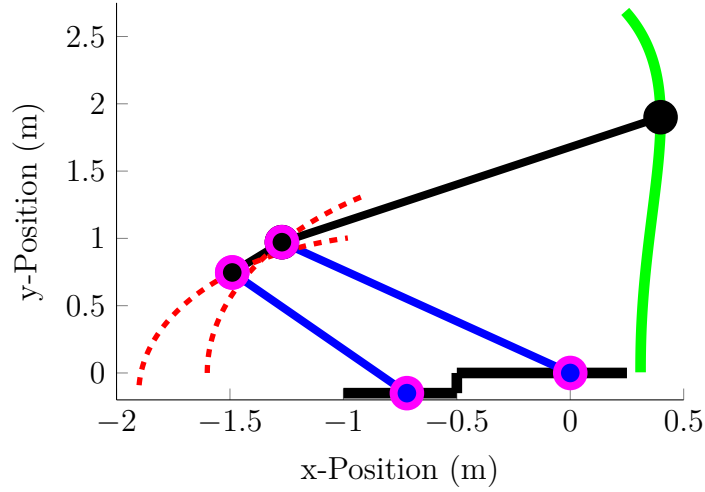


Figure 2.4: Trajectory of the cross bar when  $\varphi_1$  is varied

parts are not perfectly rigid either. To accommodate for that, the coupling rod  $l_3$  is modelled in a concentrated-parameter fashion by adding a spring/damper system at its end. The variation of length is described by the term  $\delta$  which is added to the nominal length  $l_3$  of the rod and is depicted in Figure 2.3. The equations derived so far remain valid if  $l_3$  is replaced by  $l_3 + \delta$ . Thus, a second degree of freedom is now introduced to the system which approximately captures the rod's flexibilities. Other approaches, to consider for the nonlinearities inside the pantograph are for example imperfect joints [23].

### 2.1.2 Velocity Formulation

Starting point are again the equations (2.1) and (2.2), but this time their derivatives with respect to time are computed and  $l_3$  is substituted by  $l_3 + \delta$ . This time-dependent  $\delta$  term introduces an additional degree of freedom and this leads to:

$$-l_1 \sin(\varphi_1) \dot{\varphi}_1 - l_2 \sin(\varphi_2) \dot{\varphi}_2 = -(l_3 + \delta) \sin(\varphi_3) \dot{\varphi}_3 + \dot{\delta} \cos(\varphi_3), \quad (2.15)$$

$$l_2 \cos(\varphi_2) \dot{\varphi}_2 + (l_3 + \delta) \cos(\varphi_3) \dot{\varphi}_3 + \dot{\delta} \sin(\varphi_3) = l_1 \cos(\varphi_1) \dot{\varphi}_1. \quad (2.16)$$

Solving this for  $\dot{\varphi}_2$  and  $\dot{\varphi}_3$  under the assumptions that  $\varphi_1$  and  $\delta$  are the two degrees of freedom (independent variables) yields the angular velocities

$$\dot{\varphi}_2 = \underbrace{\frac{l_1 \sin(\varphi_3 - \varphi_1)}{l_2 \sin(\varphi_2 + \varphi_3)}}_{S_2(\varphi_1, \varphi_2, \varphi_3)} \dot{\varphi}_1 + \underbrace{\frac{-1}{l_2 \sin(\varphi_2 + \varphi_3)}}_{D_2(\varphi_2, \varphi_3)} \dot{\delta}, \quad (2.17)$$

$$\dot{\varphi}_3 = \underbrace{\frac{l_1 \sin(\varphi_1 + \varphi_2)}{(l_3 + \delta) \sin(\varphi_2 + \varphi_3)}}_{S_3(\varphi_1, \varphi_2, \varphi_3, \delta)} \dot{\varphi}_1 + \underbrace{\frac{1}{(l_3 + \delta) \tan(\varphi_2 + \varphi_3)}}_{D_3(\varphi_2, \varphi_3, \delta)} \dot{\delta}. \quad (2.18)$$

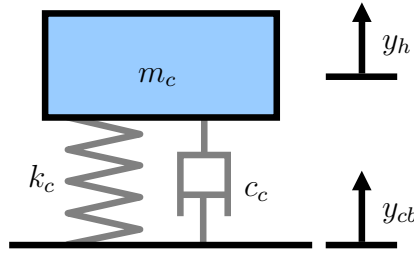


Figure 2.5: Substituted mechanical system of the collector-head (pan-heads and torsion springs) which is mounted on the cross bar

By noting that

$$\dot{\varphi}_{2,3} = \frac{\partial \varphi_{2,3}}{\partial \varphi_1} \frac{d\varphi_1}{dt} + \frac{\partial \varphi_{2,3}}{\partial \delta} \frac{d\delta}{dt} \quad (2.19)$$

it is clear that  $S_{2,3}$  and  $D_{2,3}$  are the partial derivatives of  $\varphi_{2,3}$  with respect to the two degrees of freedom  $\varphi_1$  and  $\delta$ , respectively.

## 2.2 Collector-Head

Before the equations of motion are derived, the model is completed by describing the collector-head consisting of the pan-heads and sophisticated torsion springs on top of the arrangement of rods. Here, a suitable initial model structure is a simple one degree of freedom oscillator. This is justified by the translational motion and the symmetric suspension of the torsional springs. The direct identification of this stage supports this structural choice as outlined in Chapter 4. Therefore, the transfer function is derived for the system involving the three signals: pan-head-position, cross-bar-position and force acting on the pan-head mass. The subsystem describing the collector-head is depicted in Figure 2.5 and analysing it in the Laplace domain finally yields:

$$Y_{cb}(s) - Y_h(s) = \Delta Y(s) = \frac{\frac{1}{m}}{s^2 + \frac{c}{m}s + \frac{k}{m}} F_1(s) + \frac{s^2}{s^2 + \frac{c}{m}s + \frac{k}{m}} Y_2(s) \quad (2.20)$$

The position difference  $\Delta Y$  between the cross-bar and the pan-heads is extracted from the video recordings that were made from the test-runs and will be described in Chapter 3.3 in more detail. The force acting on the pantograph is measured by a force sensor placed on the linear motor. From these data the parameters of the collector-head can be estimated, as described in Chapter 4.

## 2.3 Equations of Motion

As can be seen from Figure 2.1, the centers of gravity of the individual rods are not located at their half-length due to their non-uniform cross-sections and tapered

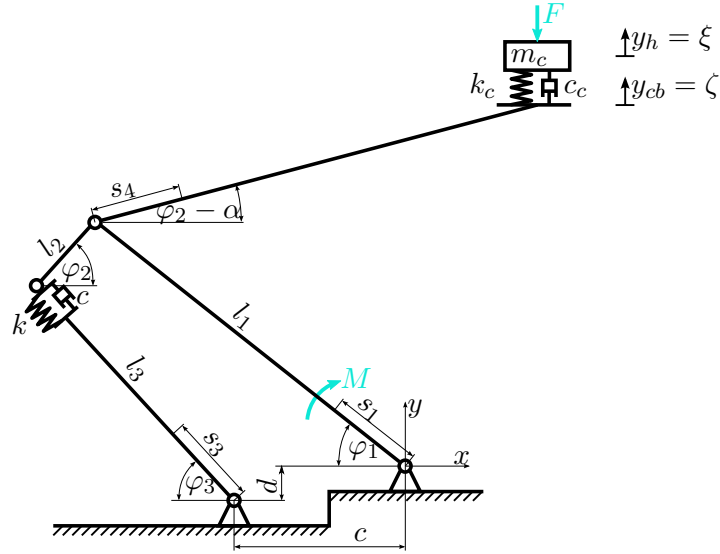


Figure 2.6: The main pantograph model used

shape. Especially the upper arm narrows towards the end. Therefore, the centroidal distances  $s_1 - s_4$  (see Figure 2.6) are considered in the modelling process for each bar and can as well be estimated later by treating them as variables and thus adding additional four parameters to the estimation problem.

The final pantograph model for which the equations of motion are derived is depicted in Figure 2.6. The centroidal distances are measured from the angle's reference hinges, and the mass moments of inertia are calculated for rods with negligible radius:

$$I_{\text{center}} = \frac{ml^2}{12}. \quad (2.21)$$

The velocity of each part's center of mass is calculated by taking their position equations (the lower arm's hinge is taken as the coordinate's system center) and deriving it with respect to time, taking in account (2.17) and (2.18), which express the velocities of the dependent angles.

The total kinetic energy  $T$  and potential energy  $V$  of the system can now be defined as:

$$\begin{aligned} T &= \frac{1}{2} \sum_{i=1}^4 \left( I_i \dot{\varphi}_i^2 + m_i v_i^2 \right) + \frac{1}{2} m_c \dot{\xi}^2, \\ V &= \frac{1}{2} \sum_{i=1}^4 \left( m_i g y_{s_i}(\varphi_1, \delta) \right) + \frac{1}{2} m_c g \xi + \frac{1}{2} k_\delta \delta^2 + \frac{1}{2} k_c (\xi - y_{cb}(\varphi_1, \delta))^2, \end{aligned} \quad (2.22)$$

where  $y_{s_i}$  are the vertical positions of the center of mass of each rod,  $\xi$  is the position of the pantograph head, the subscript  $c$  denotes the quantity as belonging to the collector-head and  $y_{cb}$  denotes the relative height of the crossbar. The angles  $\varphi_{2,3}$  as well as their derivations are dependent on the degrees of freedom  $\varphi_1$  and  $\delta$ .

To derive the equations of motion this quantities have to be plugged into the Euler-

Lagrange-equations [24]:

$$\frac{d}{dt} \left( \frac{\partial L}{\partial \dot{q}_i} \right) - \frac{\partial L}{\partial q_i} + \frac{\partial R}{\partial \dot{q}_i} = Q_i \quad (2.23)$$

to finally obtain the equations of motion. The Lagrangian Function  $L$  is defined as the difference between the kinetic and potential energy:  $L = T - V$ ,  $Q_i$  are the generalised forces and  $R$  denotes to Rayleigh's dissipation function which is defined as [25]:

$$R = \frac{1}{2} \sum_i c_i \dot{q}_i^2 = \frac{1}{2} (c_1 \dot{\varphi}_1^2 + c_2 \dot{\varphi}_2^2 + c_\delta \dot{\delta}^2 + c_c (\dot{\xi} - \dot{y}_{cb})^2). \quad (2.24)$$

It captures the velocity-dependent damping in the system. The generalised coordinates  $q_i$  are  $\varphi_1$ ,  $\delta$  and  $\xi$ .

The cumbersome task of finally deriving the equations of motion is carried out by a Maple script.

## 2.4 Linearisation

The equations of motion derived in Section 2.3 have the following form:

$$\begin{aligned} \frac{d}{dt} \mathbf{x}(t) &= \mathbf{f}(\mathbf{x}(t), \mathbf{u}(t)), \\ \mathbf{y}(t) &= \mathbf{g}(\mathbf{x}(t), \mathbf{u}(t)), \end{aligned} \quad (2.25)$$

, where the state vector  $\mathbf{x} \in \mathbb{R}^{6 \times 1}$ , the output vector  $\mathbf{y} \in \mathbb{R}^{2 \times 1}$  and the inputs  $\mathbf{u} \in \mathbb{R}^{2 \times 1}$  are:

$$\begin{aligned} \mathbf{x}(t) &= [\varphi_1, \dot{\varphi}_1, \delta, \dot{\delta}, \xi, \dot{\xi}]^T, \\ \mathbf{y}(t) &= [y_{cb}, \xi]^T, \\ \mathbf{u}(t) &= [F, M]^T, \end{aligned} \quad (2.26)$$

However,  $\mathbf{f}(\mathbf{x}(t), \mathbf{u}(t))$  comprises many nonlinear terms which are of excessive size and computationally expensive to evaluate.

Since the behaviour of the Pantograph should be investigated close to its operation point, and linear systems are much better understood than nonlinear ones, a linearisation is carried out. Therefore, an equilibrium point has to be defined in whose neighbourhood the error introduced by utilising a linear model should be small. To allow for as much flexibility as possible, no fixed values were used and the linearisation point was generically defined as:

$$\begin{aligned} \mathbf{x}_0 &= [\varphi_{10}, 0, \delta_0, 0, \xi_0, 0]^T, \\ \mathbf{u}_0 &= [M_0, F_0]. \end{aligned} \quad (2.27)$$



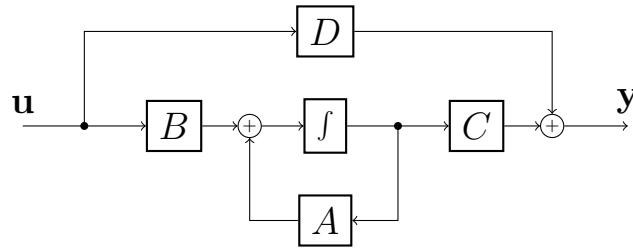


Figure 2.7: Illustration of the state space system (2.29) as a block diagram.

Expanding equation (2.25) into a Taylor series, defining  $\Delta$  as the deviation from the equilibrium point and aborting after the linear terms leads to:

$$\begin{aligned} \frac{d}{dt} \Delta \mathbf{x}(t) &= \left. \frac{\partial \mathbf{f}}{\partial \mathbf{x}} \right|_{\mathbf{x}=\mathbf{x}_0, \mathbf{u}=\mathbf{u}_0} \cdot \Delta \mathbf{x}(t) + \left. \frac{\partial \mathbf{f}}{\partial \mathbf{u}} \right|_{\mathbf{x}=\mathbf{x}_0, \mathbf{u}=\mathbf{u}_0} \cdot \Delta \mathbf{u}(t) + \mathcal{O}(\Delta \mathbf{x}^2, \Delta \mathbf{u}^2), \\ \frac{d}{dt} \Delta \mathbf{y}(t) &= \left. \frac{\partial \mathbf{g}}{\partial \mathbf{x}} \right|_{\mathbf{x}=\mathbf{x}_0, \mathbf{u}=\mathbf{u}_0} \cdot \Delta \mathbf{x}(t) + \left. \frac{\partial \mathbf{g}}{\partial \mathbf{u}} \right|_{\mathbf{x}=\mathbf{x}_0, \mathbf{u}=\mathbf{u}_0} \cdot \Delta \mathbf{u}(t) + \mathcal{O}(\Delta \mathbf{x}^2, \Delta \mathbf{u}^2), \end{aligned} \quad (2.28)$$

which is finally the linearised version of the equations of motion for the pantograph and the system can be written in the standard state-space form of a continuous time-invariant system [26]:

$$\dot{\mathbf{x}} = \mathbf{A}\mathbf{x} + \mathbf{B}\mathbf{u}, \quad (2.29)$$

$$\mathbf{y} = \mathbf{C}\mathbf{x} + \mathbf{D}\mathbf{u}, \quad (2.30)$$

where the state vector  $\mathbf{x}$ , the input vector  $\mathbf{u}$  and the output vector  $\mathbf{y}$  were already defined in (2.26). The matrix  $\mathbf{A} \in \mathbb{R}^{6 \times 6}$  is called state or system matrix,  $\mathbf{B} \in \mathbb{R}^{6 \times 2}$  is called input matrix,  $\mathbf{C} \in \mathbb{R}^{2 \times 6}$  is the output matrix, and  $\mathbf{D} \in \mathbb{R}^{2 \times 2}$  is called feedthrough matrix. A block diagram representation of the state-space system can be found in Figure 2.7.

## 2.5 Extensions to the Model

As will be shown in Chapter 4, the model depicted in Figure 2.6 has some major drawbacks and therefore some minor extensions to the model will be made. The carbon contacts are now explicitly included in the modelling process. The carbon contacts are the physical contact between the pantograph and the contact wire. They are often represented by a spring with an assumed stiffness of 50 000 N/m. This is also in agreement with certain norms (e.g. [27]) that define the quality of a catenary model. There, the pantograph is simply modelled as a two- or three-degree-of-freedom oscillator and the link between the pantograph and the wire is described as a spring. The same approach also appears in the literature, e.g. [6, 28, 29]. Figure 2.8 visualises the aforementioned model.

To obtain the corresponding equations of motion, only few adaptations had to be made to the Maple script used in Section 2.3. The potential energy  $V$  given in (2.22) of

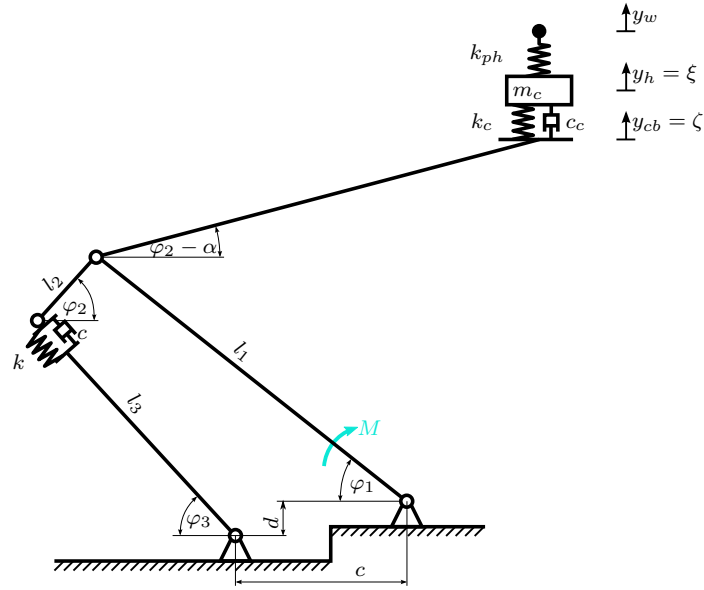


Figure 2.8: An extended pantograph model where the carbon contact is modelled as a spring

the standard pantograph model had to be expanded by a term incorporating the new spring:

$$\tilde{T} = T_{(2.22)} + \frac{1}{2}k_{ph}(\xi - \eta)^2. \quad (2.31)$$

Additionally, the force  $F$  acting on the pan-head was set to zero, and except for these minor modifications the Maple-script could be reused.

Another possibility to modify the original model is to leave the force actuation on the top unmodified and let a spring at the bottom of the pantograph create the angle-dependent uplift force [30]. The drawback of this approach is that the pressure inside the bellow is not an input to the model anymore.

## 2.6 Simple Model Structures

Many papers [3, 22, 31], as well as some norms [27], propose to model the whole pantograph as a simple two- or three-mass-oscillator. The two-mass-oscillator is depicted in Figure 2.9, and its state-space representation is:

$$\mathbf{x} = [x_1 \quad \dot{x}_1 \quad x_2 \quad \dot{x}_2]^T, \quad \mathbf{u} = [u_1 \quad u_2]^T, \quad (2.32)$$

$$\dot{\mathbf{x}} = \begin{pmatrix} 0 & 1 & 0 & 0 \\ -\frac{(k_1+k_2)}{m_1} & -\frac{(c_1+c_2)}{m_1} & \frac{k_2}{m_1} & \frac{c_2}{m_1} \\ 0 & 0 & 0 & 1 \\ \frac{k_2}{m_2} & \frac{c_2}{m_2} & -\frac{k_2}{m_2} & -\frac{c_2}{m_2} \end{pmatrix} \mathbf{x} + \begin{pmatrix} 0 & 0 \\ 0 & \frac{p}{m_1} \\ 0 & 0 \\ -\frac{k_E}{m_2} & 0 \end{pmatrix} \mathbf{u}, \quad (2.33)$$

$$y = \begin{pmatrix} 0 & 0 & k_E & 0 \end{pmatrix} \mathbf{x} + \begin{pmatrix} -k_E & 0 \end{pmatrix} \mathbf{u}. \quad (2.34)$$

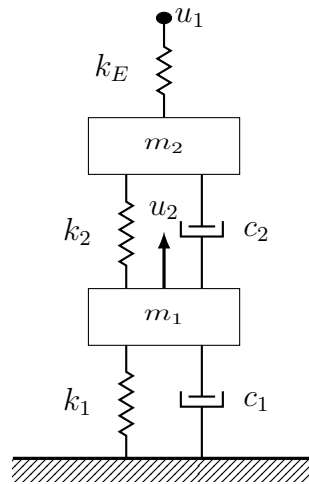


Figure 2.9: Two-mass-oscillator

The three-mass oscillator has an additional mass before the position excitation  $u_1$  and thus three additional parameters ( $m_3, k_3, c_3$ ). It has the same state-space dimension as the physical model derived in this chapter. Both oscillators will be compared to a black-box model of dimension two and three in Chapter 4.

## 2.7 Friction

Since friction occurs in every mechanical system, its influence on the pantograph's dynamics should also be briefly investigated here. The use of lubricant leads to a decrease in friction, but dependent on the actual configuration of the bearings, its effect may still be considerable. Additionally, some nonlinear effects may occur in the pantograph's dynamics that are not necessarily linked to friction but are still better described with the same approaches and thus lead to a better model.

The friction force under investigation that is responsible for a significant amount of friction phenomena in classical mechanical systems is called Coulomb's friction. Static and dynamic friction are subsumed under this term which can occur at the same time or alternating (stick-slip). Usually, the force needed to set an object in motion is higher than the one needed to keep it moving. The effect of viscous friction would in its most simple form be considered velocity-proportional and can be combined with Coulomb's friction. Figure 2.10a shows the combination of Coulomb and an additional nonlinear velocity-dependent viscous friction, as well as the effect of stiction.

For the sake of simplicity and to reduce the number of additional degrees of freedom in the identification process, both coefficients of Coulomb friction are assumed to be equal and viscous friction is neglected. This yields a friction model in the form of a scaled signum function in a plot where the abscissa represents velocity. Figure 2.10b

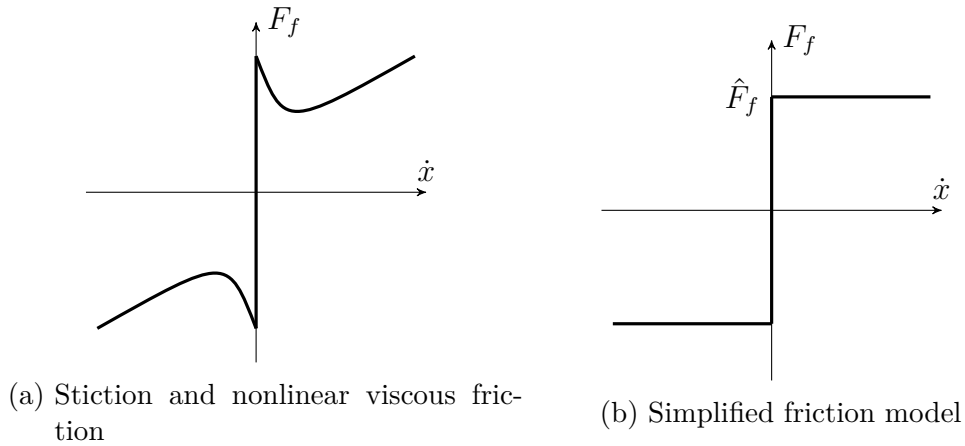


Figure 2.10: Two friction models

visualises the friction model used:

$$F_f = \begin{cases} 0 & \text{if } v = 0 \\ \hat{F}_f \cdot \text{sgn}(v) & \text{if } v \neq 0 \end{cases} \quad (2.35)$$

The simplified friction terms are added to the two-degree-of-freedom oscillator (for both masses) and thus increases the number of variables by two. Instead of the unsteady signum function in equation (2.35), the smoothed term  $\hat{F}_f \tanh(kv)$  is often used instead which, for large  $k$ , is a good approximation of the signum function, however with a bounded derivative.

The equations of motion for the two-mass-oscillator including Coulomb friction are:

$$\mathbf{x} = [x_1 \quad \dot{x}_1 \quad x_2 \quad \dot{x}_2]^T, \quad \mathbf{u} = [u_1 \quad u_2]^T, \quad (2.36)$$

$$\dot{\mathbf{x}} = \begin{pmatrix} 0 & 1 & 0 & 0 \\ -\frac{(k_1+k_2)}{m_1} & -\frac{(c_1+c_2)}{m_1} & \frac{k_2}{m_1} & \frac{c_2}{m_1} \\ 0 & 0 & 0 & 1 \\ \frac{k_2}{m_2} & \frac{c_2}{m_2} & -\frac{k_2}{m_2} & -\frac{c_2}{m_2} \end{pmatrix} \mathbf{x} + \begin{pmatrix} 0 & 0 \\ 0 & \frac{p}{m_1} \\ 0 & 0 \\ -\frac{k_E}{m_2} & 0 \end{pmatrix} \mathbf{u} + \begin{pmatrix} 0 \\ -F_{f_1}(x_1) \\ 0 \\ -F_{f_2}(x_2) \end{pmatrix}, \quad (2.37)$$

$$y = (0 \quad 0 \quad -k_E \quad 0) \mathbf{x} + (k_E \quad 0) \mathbf{u}. \quad (2.38)$$

Note that in (2.38)  $F_{f_1}(x_1)$  and  $F_{f_2}(x_2)$  comprises nonlinear terms in  $\dot{x}_1$  and  $\dot{x}_2$ , respectively and therefore render the system nonlinear, leading to a system of the form:

$$\dot{\mathbf{x}} = \mathbf{f}(\mathbf{x}, \mathbf{u}). \quad (2.39)$$

# Chapter 3

## Test Bed and Measurement Interface

The main part of the test bed in which pantographs can be analysed is made up of a six-axis industrial robot that is augmented by a linear motor to allow for fast uniaxial dynamics. With this configuration, great travelling distances are possible due to the robot, while enabling high-bandwidth motion on a small scale of about 30 cm with the linear motor. A schematic drawing of the whole test bed is shown in Figure 3.1

Unfortunately, the available robot control unit is not capable of accepting external position demand inputs but needs predefined trajectories to change its position. Therefore, for the test runs just the linear motor was used to actuate the pantograph from above. The aluminium bar should imitate the contact region of the catenary's contact wire and is mounted on the linear motor via a six-axis force and momentum sensor. It is connected to a measurement amplifier (mounted on top of the robot) where its values can be accessed. The linear motor can be accessed via a control unit via different protocols or the manufacturer's software installed on the operating computer. Two laser distance sensors were available for position measurements. Both were installed to measure the cross-bar's position to reduce the influence of measurement noise. The pantograph is lifted by a pneumatically driven actuator where the supply pressure is delivered by a 10 bar compressed air reservoir to produce the same conditions as on a real train. The pneumatic hoses are running over a panel with a simple PI-controller that adjusts the pressure inside the bellow to a constant reference. However, for the test runs a controllable valve was installed so that the pressure is freely controllable by applying an analogue voltage.

For the test runs used to acquire measurement data, the operating computer was not used. Instead, all actors and sensors were wired to the real-time platform dSPACE MicroAutoBox II (MABX). The choice was especially advantageous because the sensors operated in the range 0 to 10 V which could directly be fed into the MABX.

Additionally, different parts of the pantograph were marked with coloured adhesive labels and the test runs were recorded by a camcorder capable of capturing 50 full frames per second. Thus, a 50 Hz position measurement of several pantograph parts could be extracted as described in Chapter 3.3.

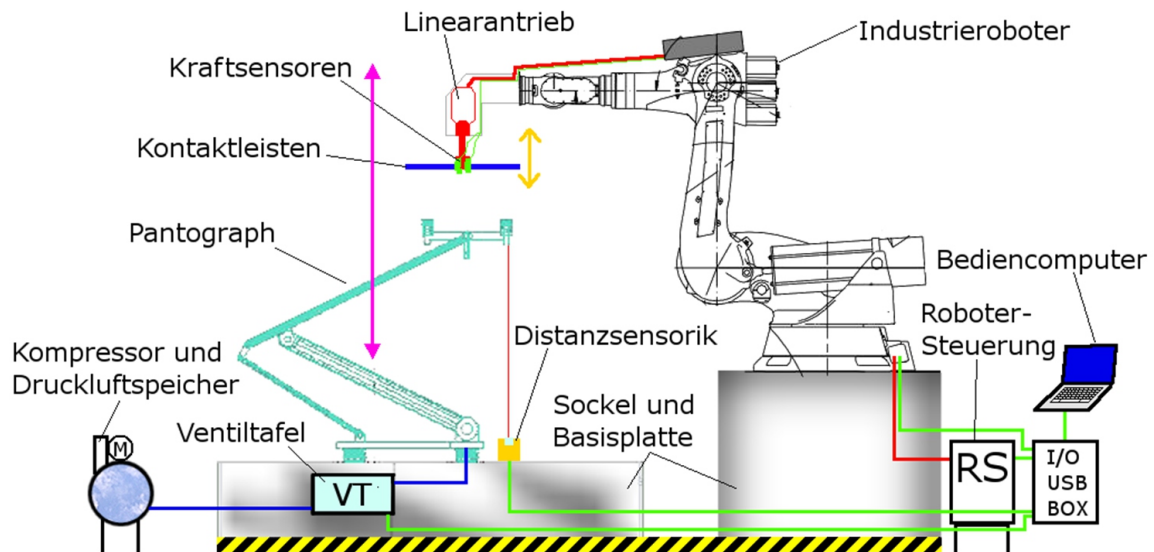


Figure 3.1: Schematic drawing of the pantograph testbed, taken from [2]



Figure 3.2: Signals processed by the MicroAutoBox II (left: Sensors, right: actuators)

### 3.1 MicroAutoBox II Interface

The dSPACE MicroAutoBox II (MABX) was originally built as a vehicle-compatible rapid prototyping system and therefore offers a rather compact and robust design. For this work it was used for data acquisition and generating actuator input values, as well as implementing a PI controller for applying specific bellow pressure values (described more in detail later in this section). The program was implemented in MATLAB/Simulink and was automatically compiled, linked and stored on the MABX. The user interface to visualise and modify certain values, such as measurements or actuator output data, was built using the dSPACE ControlDesk software. Figure 3.3 shows a screenshot of the final ControlDesk implementation used. As can be seen, various settings can be changed on the fly and different output signals with a variety of options can be selected. For both the linear motor and the pneumatic bellow the following signals with the given parameters were available:

**constant** A constant value is sent every sampling instant. This value also acts as an offset and is added to every signal specified below

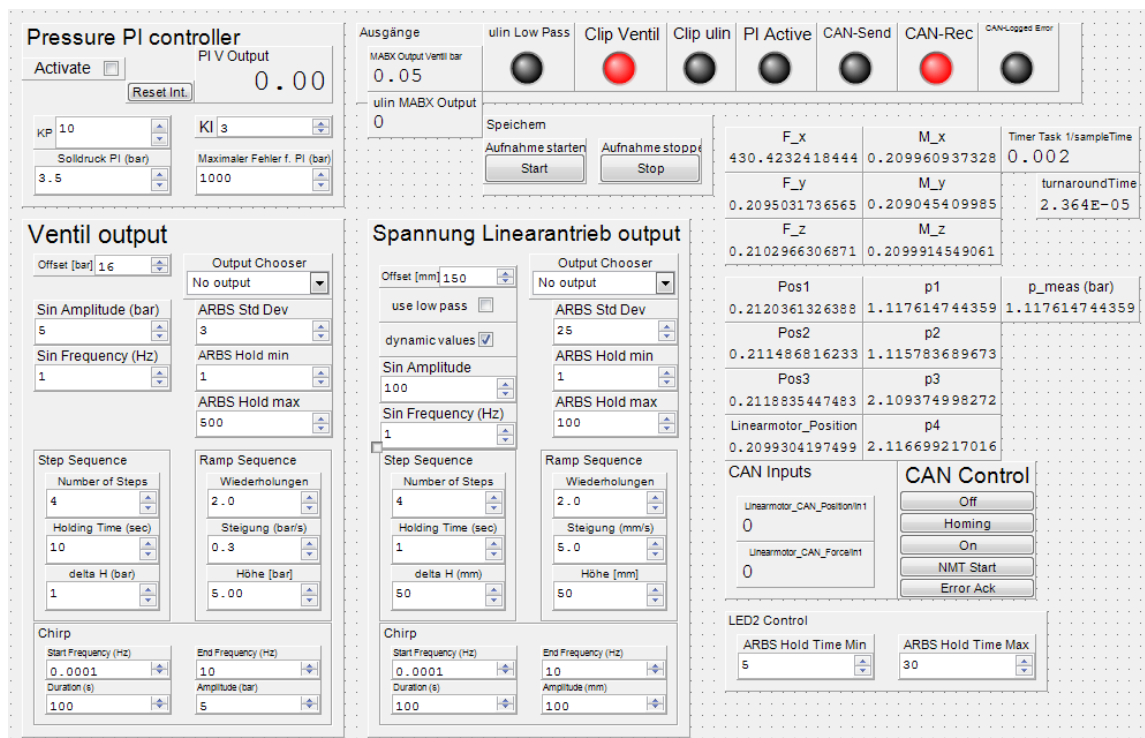


Figure 3.3: Screenshot of the developed ControlDesk GUI

**sine** (frequency, amplitude) sine wave with adjustable frequency and amplitude

**chirp** (start and stop frequency, duration, amplitude) frequency sweep from adjustable start and end frequencies to generate broadband signals.

**APRBS** (standard deviation, minimum and maximum holding time) A piecewise constant, random signal (APRBS, Amplitude-modulated Pseudo Random Binary Signal) with varying holding times and the size of the step determined by a zero-mean normal distribution with given standard deviation [32].

**ramps** (repetitions, height, gradient) freely configurable ramp signal

**steps** (count, height, holding time) freely configurable step sequence

For the linear motor, an additional input sequence was created from a numerical simulation (see [33] for details) of the catenary system of a train drive at 300 km/h that captures the distance between support wire poles (assumed to be 60 m). The sequence is therefore 0.72 s long and periodic. Its visualisation is shown in Figure 3.4. Buttons for starting and stopping the data capturing process and also for generating the selected output signals were realised via the built-in trigger functions of ControlDesk.

Large steps in the linear motor position demand signal should be avoided so as not to impose too much stress on the pantograph because they often lead to loss of contact

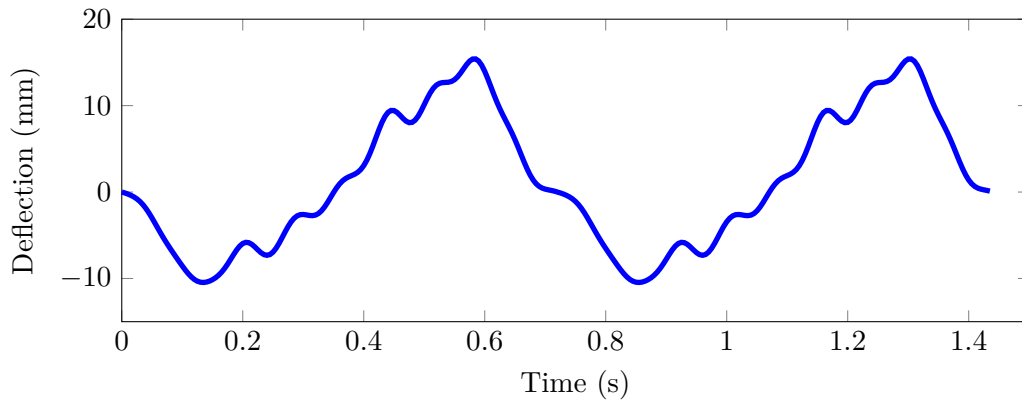


Figure 3.4: Contact wire deflection (two periods from a simulation) of a simulated catenary/pantograph interaction (train speed 300 km/h, passive pantograph).

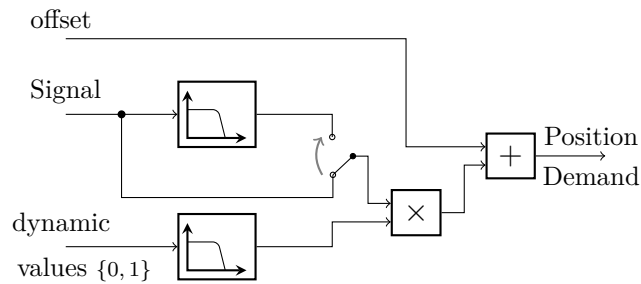


Figure 3.5: Illustration of the signal processing before the position demand command is sent to the linear motor.

and therefore pan-head wear. Besides, the linear motor software quits with an error message when the position error is too large. To avoid this situation a reference signal low-pass filter can be activated. Additionally, the dynamic part of the output signal (i.e. before the offset is added) is multiplied by a low-pass-filtered variable called *dynamic values* which can be switched between zero (just constant output) and one (selected output is unmodified). This is helpful if, for example, the frequency of a sine signal is altered, which would normally cause a jump in the output if the dynamic values variable is set to 1. By temporarily setting it to zero, the dynamic part is softly driven to zero as well, because the signal is being multiplied by a low pass filtered step function. Now, unsteady behaviour in output signals is of no consequence and the settings can therefore be changed safely. Turning the normal low-pass-filter on and off would lead to steps because of the discontinuous changes in signal phase lag. The whole process of processing the output signal to the linear motor is illustrated in Figure 3.5.

The linear motor was addressed via the CAN-Bus with an effective sampling rate of 250 Hz. Every second message had to be a synchronisation sequence. Since the normal position demand command was only usable for up to approximately 50 Hz, a mode called *Position-Stream* was used. With this command the linear motor's



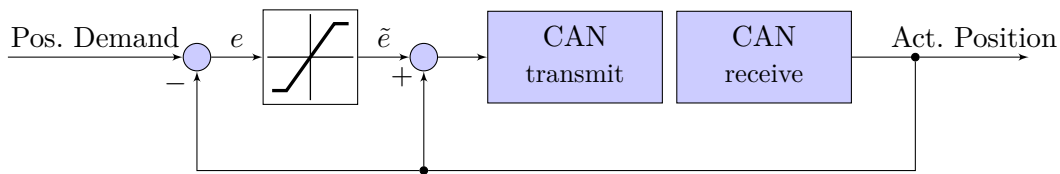


Figure 3.6: Logics used to limit the maximum position error per sample for the linear motor

internal high-level controller is ignored and only position errors between the demand and the current position of up to 30 mm are allowed before the linear motor control drive quits with an error message and has to be restarted. To circumvent this, the logics depicted in Figure 3.6 was used to limit the position error per sample to a maximum of 5 mm.

Since the pneumatic bellow has very limited dynamics and approximately acts as a first-order low-pass element, no sophisticated output signal conditioning is necessary. For setting a given pressure an adjustable valve that had a 10 bar input and was able to provide 0 bar to 7.5 bar at the output depending on a control voltage in the range 0 V to 24 V was used. Alternatively — as first suggested by the manufacturer — a 24 V PWM signal can be used. This was first tried by connecting the voltage drive pin of the MABX to 24 V and using a digital output with a PWM signal. However, it turned out that the valve attempts to draw actuation power from this signal but the MABX was not able to provide sufficient current to drive the valve. The chosen solution was to use an external power supply unit with a controllable output voltage to drive the valve. After surveying the input/output behaviour, a nonlinearity and a deviation between the load and the open loop voltage was observed. Unfortunately, because of a ground loop due to the required circuit wiring, it was not possible to measure the output voltage of the power supply unit with the MABX on a voltage divider. The chosen workaround was to control the bellow pressure with a simple PI Controller. This can be seen as an outer feedback loop since the valve voltage input directly affects the pressure. Again, the user can enable or disable the controller and tune its parameters from inside ControlDesk.

The third output signal is a pseudorandom binary sequence (i.e. a sequence that can only take values 0 and 1, but each time with different, random hold periods). It is used to drive an LED needed to synchronise the MABX measurements with the video recordings. This is described more in detail in Section 3.2.

## 3.2 Video Position Measurement and Synchronisation

The pantograph is equipped with coloured labels, and a FullHD camera, capable of recording 50 full images per seconds with an adjustable shutter time, was positioned in front of the pantograph to capture the collector-head including the pan-heads in the full area of operation of the linear motor. The shutter time is chosen with 2 ms

to match the sampling time of the MABX which, in turn, made the video a little darker because the incoming light was reduced. This allows to determine precisely whether the LED has been activated or not in a particular “fine” sampling interval (for each frame).

After the test runs, the video recordings were postprocessed on a PC where the marker positions were extracted and the pixels position were converted to millimeters. With this procedure, the relative position of the given parts is available, but in order to reconstruct their absolute positions, their distance from the ground or a hinge on the pantograph’s frame was measured at the test bed and utilised as offset to yield absolute positions.

For synchronizing the 500 Hz measurements and the 50 Hz camera recordings a pseudorandom binary sequence (holding time between 5 ms and 30 ms) was used as one of the MABX digital outputs to light up an LED that was also recorded by the camera. So parts of the same synchronisation signal (cropped at the beginning and the end since the recording and the MABX data capturing were not started at exactly the same time) were available at two different sampling intervals. The lower sampled camera signal of course is missing some bit flippings due to the short holding time of the LED bitstream. Assuming no bit errors in the camera recording’s extracted LED sequence, one out of 10 samples of the MABX output sequence is available (sampling rate is ten times higher). If the cross-correlation between the downsampled MABX bit stream and the camera LED sequence is built, one gets a result similar to Figure 3.8a. A single peak is obtained, meaning that both signal are shifted by 1237 coarse sample instants. However, it is possible to get a more accurate information in the fine time grid.

A short example of a pseudorandom binary sequence is shown in Figure 3.7. There, it is also shown that at least for short signals, it is not possible to exactly reconstruct at which time instant (of the faster sampled signal) the video recording was started. In this figure, the measurement process was started at  $t = 0$  s and  $t = 0.01$  s, respectively, and both variants lead to exactly the same bit stream with respect to the slower sampled signal.

In order to accurately synchronise the two measurements at first the autocorrelation of the camera measurement is built to obtain a possible maximum value for the (normalised) cross-correlation that is going to be built and quantify the level of it from 0 (no (linear) dependency at all) to 1 (perfect linear fit). Now the MABX LED signal is downsampled ten times, where each time the starting bit is shifted by one. Next, for each of these resampled signals the cross-correlation to the LED signal extracted from the video recordings is built. A possible outcome of one cross-correlation function call is shown in Figure 3.8a, where artificially 10 % of the bits were flipped to demonstrate the method’s robustness. For each of the ten cross-correlation function one single peaks exist, but its value varies. This is demonstrated in Figure 3.8b where the value of the peak is plotted for each of the ten downsampled MABX LED sequences. The optimal time shift on the MABX time base can then

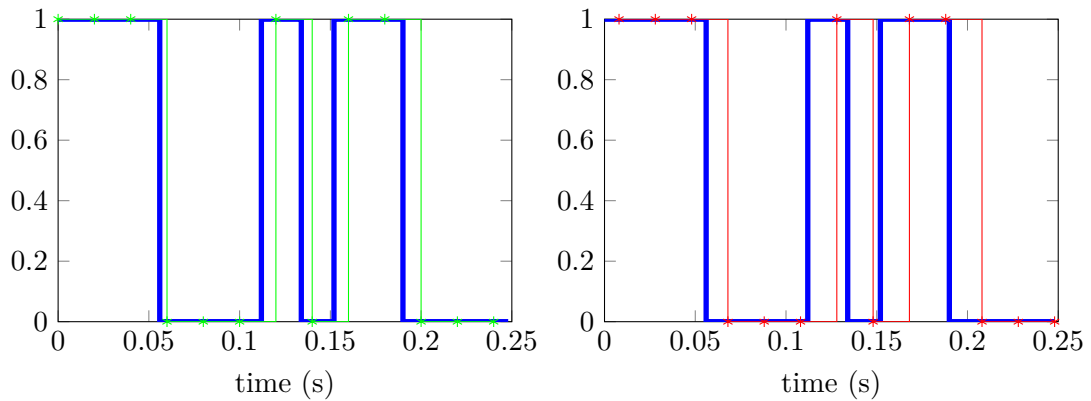


Figure 3.7: An extract of the LED synchronisation signal sent by the MABX (blue) and two slower sampled camera measurements (green and red) starting at slightly different instants of time that lead to exactly the same sequence

be calculated with:

$$t_{\text{shift}} = \text{lags} \times \frac{T_{\text{camera}}}{T_{\text{MABX}}} + i - 1, \quad (3.1)$$

where  $i$  is the number between 1 and 10 for which the cross-correlation function yielded a maximum. The fraction results to 10 in this case (number of finer samples per coarse sample) and lags means the number of lags in the coarse time grid (1237, obtained from the left subfigure) that led to the optimum value for the cross-correlation function and the subtraction of 1 is necessary because MATLAB indices start with 1.

Afterwards the longer signal is cropped so both — the camera position extraction and all the MABX measurements — have exactly the same size (i. e. samples). To warrant that no information is lost, the signals extracted from the camera recordings are upsampled.

The application of the whole process of data capturing, video post processing and synchronisation is described in Chapter 3.3.

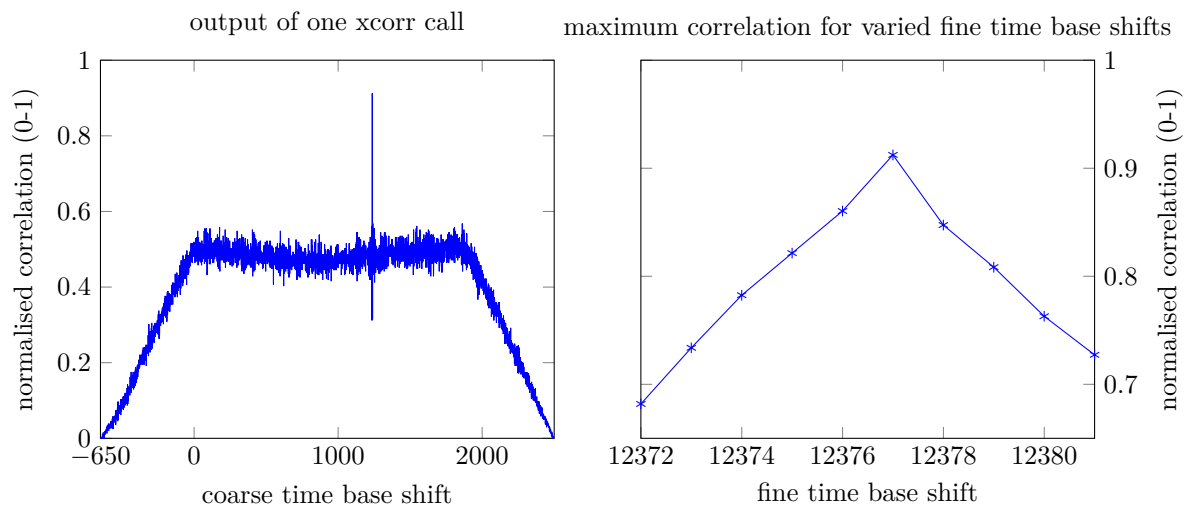


Figure 3.8: Results of the correlation analysis. The value of 1 (perfect correlation) was not reached because 10% of the camera bits were artificially flipped. The left plot shows the result of the cross-correlation between the downsampled MABX LED sequence and the camera recording. The right plot shows that it does matter which of the ten first fine data points is the starting sample of the downsampling.

## 3.3 Extracting Position Measurement from Camera Recording

At first the only position measurements available at the test bed were two laser sensors. However, their output signal was heavily corrupted by noise. Beside that, the positioning of the sensors turned out to be rather complicated because of the horizontal movement depicted in Figure 2.4 on page 9 of the collector-head during a height change and only the cross bar's position was measureable with arguable effort. However, the lasers were adjusted to measure the position of the airfoils attached to the crossbar, also introducing a small (but probably negligible) error that was accepted in favour of the easy positioning.

In order to receive more location information — especially about the pan-heads and the cross bar — labeled markers were attached to different parts of the pantograph and the test runs were recorded by a Full HD recorder with 50 frames per second and a shutter time of 2 ms, matching the MABX sampling frequency of 500 Hz for reliable detection of the synchronisation LED's status.

### 3.3.1 Conversion Process

For processing the video files in MATLAB, an extension called *VideoUtils*<sup>1</sup> was used. It allows to read, write and modify every single frame of the recording as a  $1920 \times 1080 \times 3$  double array. So every pixel's color information is easily accessible for each frame.

The marker detection, which is based on a proof of concept done by Alexander Schirrer, is based on blob detection and some a priori effort is required to define the approximate location and color of each marker.

For this task a setup routine was created and the chosen settings were checked with early and later measurements to account for day light changes. First, for every marker the area in which it is expected to lie had to be selected. This procedure is depicted in Figure 3.9.

Then, an area inside the colored marker had to be selected, and the average color content of the read, green and blue contributions inside this region is calculated. This is because the specific color gradients inside the marker may change depending on the illumination. Also, it is very unlikely that two pixels have exactly the same color.

Next, a threshold value has to be specified that is comparable to a tolerance value with which the color calculated should be met in the image procession. Setting it to a low value will result in a generous detection barrier, but would lead to a more noisy signal and most likely to false detections, too. E.g. a darker region might then be mistaken as dark green causing the marker's position to jump. The higher the threshold value, the more precisely the color values have to match each other in order to define the pixels as belonging to the marker. This may lead to no positive results at all.

---

<sup>1</sup><http://sourceforge.net/projects/videoutils/>

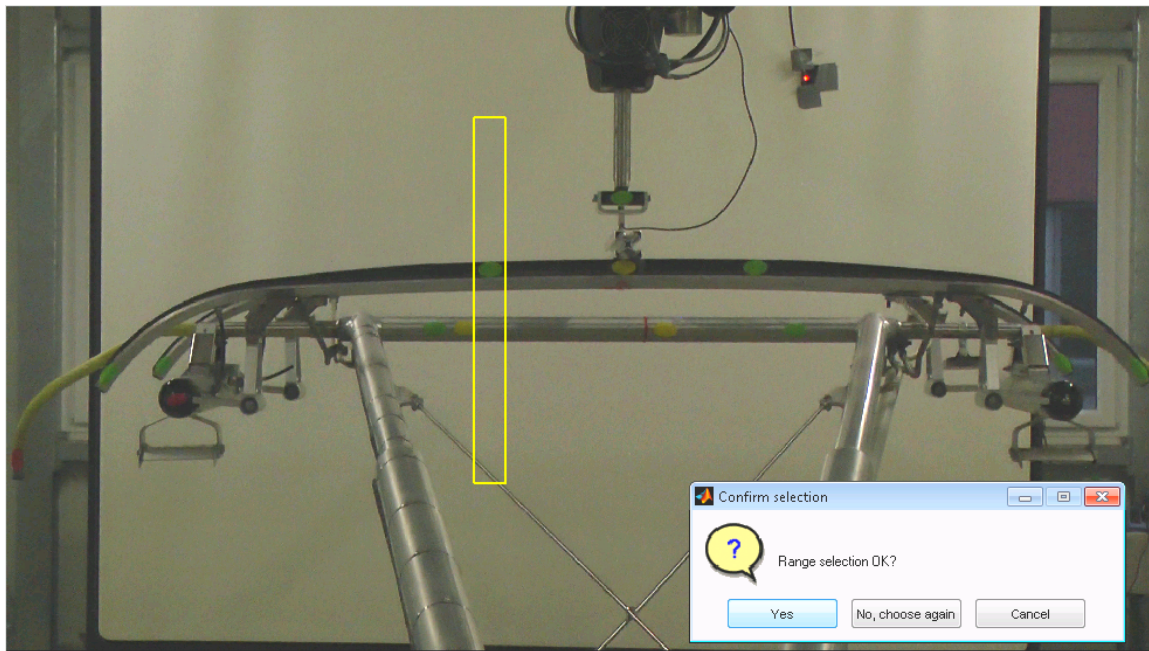


Figure 3.9: Setting up a region inside which the marker is expected to remain

For each marker, the following steps have to be repeated to detect its position, where all steps are repeated for each frame of the video and of each pixel the color contents (red, green, blue) have to be available:

1. Subtract the red, green and blue values of the marker color from each pixel;
2. create a gray-scale picture by taking the norm of the red, green and blue contribution value and subtracting the result from 1;
3. maximise the saturation, so that areas with the marker color should stay white (saturation 1) and all others are darkened as much as possible;
4. check each saturation value against the user-defined threshold value. If it is larger, set it to 1, otherwise to 0. The result is a binary image;
5. use the built-in MATLAB function *imopen* to morphologically open an image and automatically remove all white areas that are smaller than a disk with a radius of 2 pixels. This filters out smaller disturbances coming, for example, from measurement noise or objects behind the window which was partly on the recording area;
6. compute the center of the remaining white pixels and store it as the marker's position.

Figure 3.10 shows each of these steps for the pre-defined area for one green marker attached to the pan-heads. The darker region below the pan-heads is the cross bar.

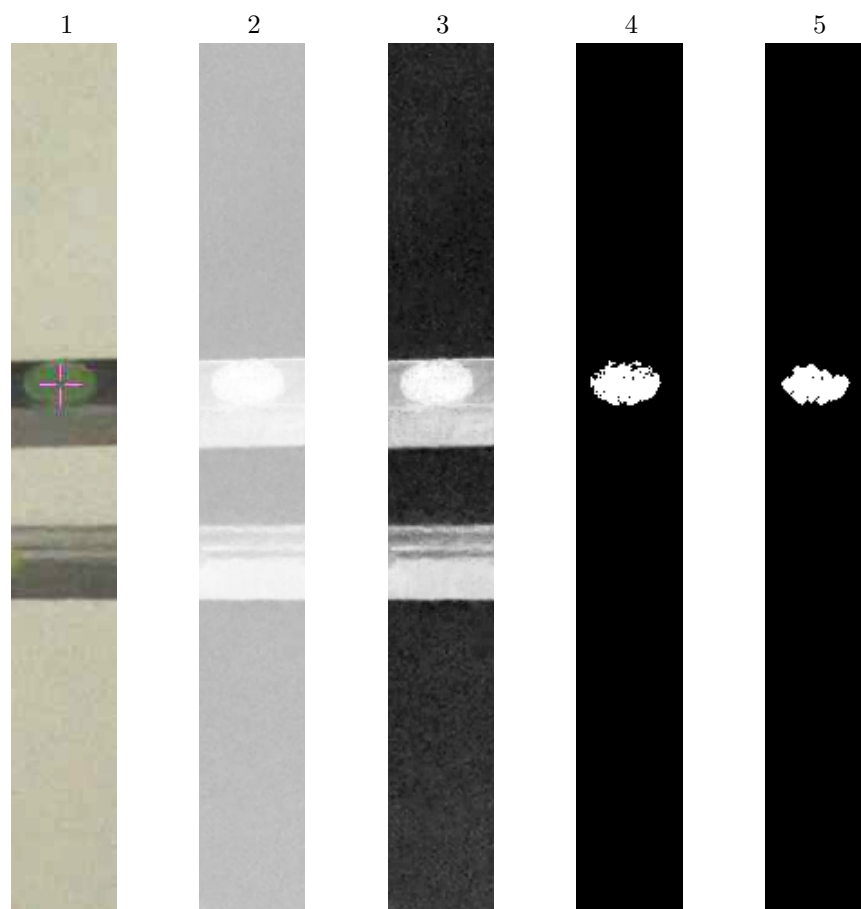


Figure 3.10: Steps of the marker detection process

Unfortunately, for the second test runs no spot lights were available. This imposed a problem on extraction of some marker's position, as they were occasionally in the shadow of parts of the pantograph. For example the yellow marker attached at the center of the pan-head was skipped for the position extraction since its coloring changed too much between the upper and lower linear motor's position.

As can be seen in Figure 3.9, a white screen, however appearing grey in the picture, was positioned behind the pantograph to increase the contrast between the marker, respectively the pantograph and the background. The synchronisation LED was attached on this screen so that its position remained unchanged during the test runs and it was not covered by the pantograph. For the detection of the LED's status only the pixels around the diode were checked. If the maximum of the red contribution of one pixel exceeded 0.7 (of a maximum of 1) then the LED was assumed to shine. After processing the whole video, the marker's positions were available in pixel coordinates in Full HD resolution. A factor for converting them to mm was obtained by holding an object with a known length right beside each marker and calculating the ration between the objects length and its pixel representation in the video.

Then, as already described in section 3.2, the autocorrelation between the camera's LED extraction and the decimated (here only every 10<sup>th</sup> value was used) MABX LED output signal was built, were the decimation started at different positions to get the optimal shift value. Then the upsampled video position measurement and the MABX recordings can be synchronised and the longer one appropriately cropped so they conform to each other. Afterwards they are stored in one mat-file to represent one measurement that can be used for the parameter estimation process.

### 3.3.2 Comparison of Different Sensors

In this section, the available position signals are compared. For the first test runs no position feedback from the linear drive was available and the laser sensors were positioned vertically under the airfoils. These sensors were not used anymore for the second part of the test runs, but a CAN-Interface to the linear drive was available instead. This has the advantage of digital data transmission and eliminates transmission noise.

In Figure 3.11 the two position signals obtained from the laser sensors are shown, as well as the extraction from the camera recordings of the pan-head's position. Although the signal from the two laser sensors appears very noisy it is possible to see its conformity with the video extraction. If the laser sensor signal is sent through a low-pass filter, the result is also usable for estimating the parameters of the pantograph model.

In Figure 3.12 the position signal of the linear motor's slider received from the linear motor's control unit via the CAN-Bus is displayed together with the extraction of the slider's position from the camera recordings. The latter signal is more overlaid with noise but in general the agreement between both signals is good.



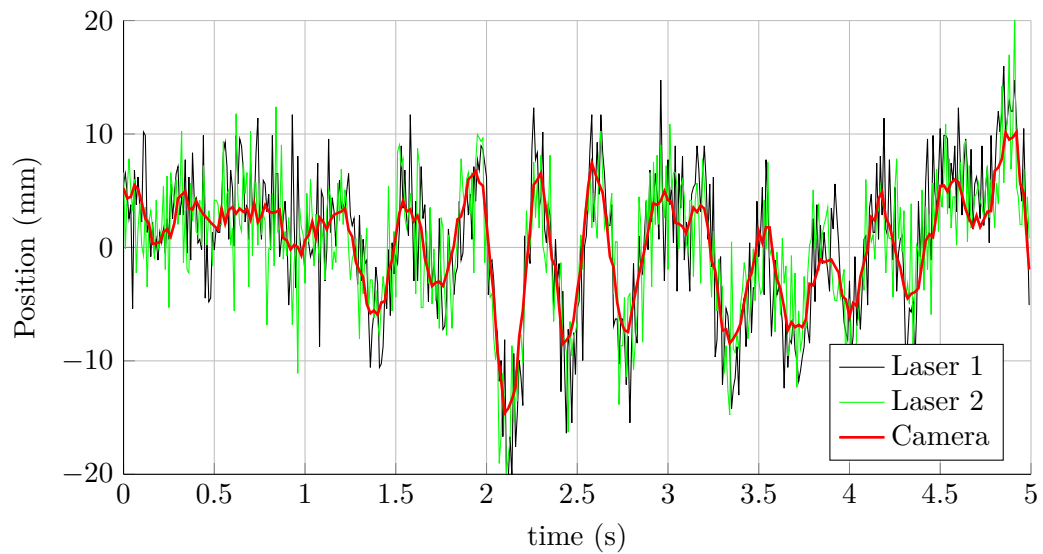


Figure 3.11: Extracted measurement of the cross-bar position and the signals of the two laser sensors.

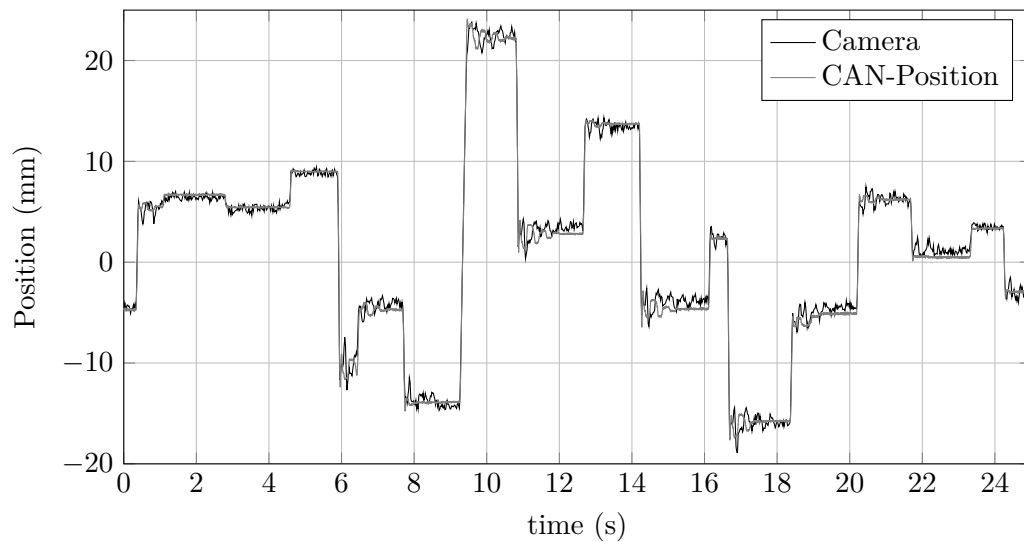


Figure 3.12: Linear motor's slider position received via CAN-bus (gray) and the extracted position signal from the video recordings (black).

# Chapter 4

## Identification Process

This chapter describes the process of estimating the unknown parameters in the equation of motion (2.28). For this purpose, two test runs were made on the pantograph test bed. The recordings from the MABX are synchronised to the position extracted from the video recordings (with the procedure described in Chapter 3). The prepared data sets are suitable for a reliable parameter identification process.

First, basic theory on parameter identification and the possible (mathematical) approaches are given before the actual process is described. Initial data investigations are discussed. Finally, the obtained models are validated and their quality is quantified and discussed.

### 4.1 Theoretical Background

During the parameter estimation process the model structure is assumed to stay constant. For each model structure described in Chapter 2, one of the identification processes described in this section is carried out. The aim of model identification here is to obtain valid (i.e. well-performing and physically plausible) values for the unknown pantograph parameters in the model.

The actual structure of the model (e.g. linear or nonlinear, number of states, ...) does not matter for the presented identification method as long as the model's input/output dynamics matches the identification data obtained from the measurements.

Mathematically, the model is given in the following generic form:

$$\mathbf{y} = f(\mathbf{u}, \boldsymbol{\theta}) \quad (4.1)$$

where  $\boldsymbol{\theta}$  denotes the vector of unknown parameters that are going to be estimated,  $\mathbf{u}$  is the input into the model and  $\mathbf{y}$  is the model output. All quantities are vectors and the general MIMO (Multiple Input Multiple Output) case is considered. It is assumed that a sufficiently long series of measurements is available with equidistant time sampling. For compact notation, a measurement sequence is collected into one vector

$$\mathbf{Z}^N = [\mathbf{y}^T(1), \mathbf{u}^T(1), \mathbf{y}^T(2), \mathbf{u}^T(2), \dots, \mathbf{y}^T(N), \mathbf{u}^T(N)]^T,$$

also called training data, which is used for the identification process. A different measurement sequence is then used for model validation. Mathematically speaking, a mapping from the data set  $\mathbf{Z}^N$  to a set of all possible model parameters  $D_{\mathcal{M}}$  is sought [34]:

$$\mathbf{Z}^N \rightarrow \hat{\boldsymbol{\theta}} \in D_{\mathcal{M}},$$

and this mapping is called a parameter estimation method.

The goal of the identification is to minimise a user-defined error function  $\boldsymbol{\varepsilon}$  by finding an optimal parameter estimate  $\hat{\boldsymbol{\theta}}$ . In the literature (as well as in this case) the prediction error method is often used, which means that a norm (usually the quadratic norm) of the prediction error vector

$$\boldsymbol{\varepsilon}(t_n, \boldsymbol{\theta}) = \mathbf{y}(t_n) - \hat{\mathbf{y}}(t_n | \boldsymbol{\theta}) \quad (4.2)$$

is to be minimised. Some extensions to this approach exist, including prefiltering  $\boldsymbol{\varepsilon}$  with a chosen filter  $L$ , introducing frequency weighting, or considering other norms than the quadratic norm to improve robustness against bad data or outliers.

If the quadratic norm is used on the error function  $\boldsymbol{\varepsilon}$ , the following cost function is obtained:

$$V_N(\boldsymbol{\theta}, \mathbf{Z}^N) = \frac{1}{N} \sum_{n=1}^N \frac{1}{2} \boldsymbol{\varepsilon}^2(t_n, \boldsymbol{\theta}) \quad (4.3)$$

which is to be minimised with respect to the model parameters  $\boldsymbol{\theta}$ . There are  $N$  measurements available for the identification process and each value is treated equally (the infinity norm for example would only consider the largest value). The formal optimisation criterion to retrieve the optimal parameter vector  $\hat{\boldsymbol{\theta}}$  is the solution of the nonlinear least-squares problem (4.3):

$$\hat{\boldsymbol{\theta}} = \arg \min_{\boldsymbol{\theta}} V_N(\boldsymbol{\theta}, \mathbf{Z}^N). \quad (4.4)$$

Additionally, inequality constraints such as limitations of parameter values, output amplitudes, as well as their rate of change can be incorporated into the optimisation problem.

### 4.1.1 Gradient-Based optimisation

Because of the complexity and the nonlinearity of the problem at hand, there is no obvious way to obtain the optimal solution in closed form, so iterative schemes are applied instead. The idea is to start at a chosen initial parameter vector  $\hat{\boldsymbol{\theta}}^{(0)}$ , obtained for example by an educated guess or by randomisation and iteratively improve the solution:

$$\hat{\boldsymbol{\theta}}^{(i+1)} = \hat{\boldsymbol{\theta}}^{(i)} + \mu^{(i)} \mathbf{f}^{(i)}. \quad (4.5)$$

One way to do so is by using so-called gradient methods. These widely adopted optimisation routines are usually based on evaluating the linearisation of (4.3) in the neighbourhood of the current guess  $\hat{\boldsymbol{\theta}}^{(i)}$  [34]:

$$V_N(\boldsymbol{\theta}, \mathbf{Z}^N) \approx V_N(\hat{\boldsymbol{\theta}}^{(i)}, \mathbf{Z}^N) + \left[ \boldsymbol{\theta} - \hat{\boldsymbol{\theta}}^{(i)} \right]^T \left. \frac{\partial V_N(\boldsymbol{\theta}, \mathbf{Z}^N)}{\partial \boldsymbol{\theta}} \right|_{\boldsymbol{\theta}=\hat{\boldsymbol{\theta}}^{(i)}}. \quad (4.6)$$

The gradient of the cost function in (4.6) points into the direction of the steepest slope of the cost function with respect to the parameter vector  $\boldsymbol{\theta}$ . The search direction  $\mathbf{f}$  in (4.5) is thus taken as the negative gradient:

$$\mathbf{f}^{(i)} = -\left. \frac{\partial V_N(\boldsymbol{\theta}, \mathbf{Z}^N)}{\partial \boldsymbol{\theta}} \right|_{\boldsymbol{\theta}=\hat{\boldsymbol{\theta}}^{(i)}}, \quad (4.7)$$

leading to the gradient-descent method and, with an appropriately chosen step size  $\mu^{(i)}$ , a reduction of the cost function in each step is possible. This is carried out until a local minimum is reached. This result can also be written in terms of a perturbation  $\mathbf{h}$  of the current parameter guess  $\hat{\boldsymbol{\theta}}^{(i)}$ :

$$\mathbf{h}_{\text{gradient-descent}} = \mu \frac{\partial V_N(\boldsymbol{\theta}, \mathbf{Z}^N)}{\partial \boldsymbol{\theta}} (\mathbf{y} - \hat{\mathbf{y}}). \quad (4.8)$$

In the gradient-based optimisation methods the derivation of the model output has to be computed for each parameter direction in every iteration process either numerically or, if possible, analytically. This is especially time-consuming for higher-order models. A major drawback of all gradient-based optimisation algorithms is that they only converge towards a local optimum near the current parameter guess. In addition, several extensions to this procedure exist to improve their performance. One is to iteratively adapt the step size  $\mu^{(i)}$  to higher values if the cost function is only slightly changing in the neighbourhood of the current guess. Another possibility is to take the second-order approximation of the cost function equation (4.3) (the Hessian) as the basis of the process.

### Gauss-Newton Algorithm

A well-performing second-order method is the Gauss-Newton algorithm. Its efficiency for many problems stems from its second-order of convergence, and from the fact that the Hessian matrix is approximated efficiently. Here, only a short derivation of the method will be given because it will be shown later that it is a special case of the Levenberg-Marquardt algorithm that will be discussed in the next Section.

The output of the model  $\hat{\mathbf{y}}$  using a perturbed parameter vector is approximately:

$$\hat{\mathbf{y}}(\hat{\boldsymbol{\theta}} + \mathbf{h}) \approx \hat{\mathbf{y}}(\hat{\boldsymbol{\theta}}) + \frac{\partial \hat{\mathbf{y}}(\hat{\boldsymbol{\theta}} + \mathbf{h})}{\partial \hat{\boldsymbol{\theta}}} \mathbf{h} = \hat{\mathbf{y}} + \mathbf{J}\mathbf{h}, \quad (4.9)$$

where  $\mathbf{h}$  denotes the perturbation of the parameter vector,  $\hat{\mathbf{y}}$  is from now on the output of the model with the current parameter guess and the Jacobian (gradient of the model output with respect to the parameter vector) is now written as  $\mathbf{J}$ . The perturbed model output of (4.9) can now be substituted into the definition of the cost function (4.3) and leads to:

$$V_N(\boldsymbol{\theta} + \mathbf{h}, \mathbf{Z}^N) \approx \mathbf{y}^T \mathbf{y} + \hat{\mathbf{y}}^T \hat{\mathbf{y}} - 2\mathbf{y}^T \hat{\mathbf{y}} - 2(\mathbf{y} - \hat{\mathbf{y}})^T \mathbf{J}\mathbf{h} + \mathbf{h}^T \mathbf{J}^T \mathbf{J}\mathbf{h}. \quad (4.10)$$

The derivative of the obtained cost function with respect to  $\mathbf{h}$  is set to zero

$$\frac{\partial V_N(\boldsymbol{\theta} + \mathbf{h}, \mathbf{Z}^N)}{\partial \mathbf{h}} \approx -2(\mathbf{y} - \hat{\mathbf{y}})^T \mathbf{J} + 2\mathbf{h}^T \mathbf{J}^T \mathbf{J} \stackrel{!}{=} 0 \quad (4.11)$$

and this leads to a current optimal perturbation  $\mathbf{h}$ :

$$\left(\mathbf{J}^T \mathbf{J}\right) \mathbf{h}_{\text{Gauss-Newton}} = \mathbf{J}^T (\mathbf{y} - \hat{\mathbf{y}}) \quad (4.12)$$

A comparison of (4.8) and (4.12) already shows that the Gauss-Newton method is related to the basic gradient-based optimisation algorithm described in the last Section. The main advantage of the Gauss-Newton method is its very fast local convergence [35]. On the other hand, the method converges slowly or sometimes not at all if the initial guess is far away from a minimum.

### Levenberg–Marquardt Algorithm

Beside the incorporation of higher-order terms in (4.6) there are other possibilities to improve the first-order gradient-based optimisation algorithms described above. One of these approaches is called *Levenberg–Marquardt algorithm*, also known as damped least-squares.

Levenberg [36] suggested that an additional damping term should be added to (4.12), leading to:

$$\left(\mathbf{J}^T \mathbf{J} + \lambda \mathbf{I}\right) \mathbf{h}_{\text{Levenberg}} = \mathbf{J}^T (\mathbf{y} - \hat{\mathbf{y}}), \quad (4.13)$$

where  $\mathbf{I}$  is the identity matrix,  $\lambda$  is a non-negative damping factor which is being adjusted in each iteration of the algorithm. If  $\lambda$  is large (as usually initialised) (4.13) resembles the gradient-descent method (4.8). On the other hand, if the method slowly converges to a solution,  $\lambda$  is reduced and thus the Gauss-Newton method is obtained, leading to rapid local convergence.

Marquardt [37] suggested the following extension to (4.13):

$$\left(\mathbf{J}^T \mathbf{J} + \lambda \text{diag}(\mathbf{J}^T \mathbf{J})\right) \mathbf{h}_{\text{LM}} = \mathbf{J}^T (\mathbf{y} - \hat{\mathbf{y}}), \quad (4.14)$$

called the Levenberg–Marquardt algorithm. Here,  $\text{diag}(\mathbf{J}^T \mathbf{J})$  creates a diagonal matrix consisting of the diagonal elements of  $\mathbf{J}^T \mathbf{J}$ . This way the estimated local curvature information of the cost function is incorporated in the optimisation process. With this addition even in the case of small gradients fast convergence is possible. Loosely speaking, with the Levenberg–Marquardt algorithm a large reduction of the cost function within one iteration is only possible if the perturbation  $\mathbf{h}_{\text{LM}}$  of the current parameter vector is not too large. This is done because the approximations of the cost function in the Gauss-Newton algorithm are only valid within a small neighbourhood of the current parameter guess  $\hat{\boldsymbol{\theta}}$ . This method combines the robustness properties of the gradient-descent method (4.8) with the fast local convergence of the Gauss-Newton algorithm (4.12).

In this work the Levenberg–Marquardt algorithm is used to solve a system of non-linear equations of the form:  $\mathbf{F}(\mathbf{x}) = \mathbf{0}$ , as will be described later.

### 4.1.2 Genetic Algorithm

The second optimisation method tested and finally used are the so-called genetic algorithms. They belong to the class of evolutionary algorithms that are based

on the evolution of the solution candidates by a methodology inspired by natural evolutionary processes. Their great advantage is that no derivatives of the cost function have to be calculated. Thus, they can be used on non-smooth problems with several local optima.

At the start of the optimisation process a set of solution candidates is created and initialised with random parameters that stay inside a predefined range. At each iteration step, the cost function for each individual is evaluated and the population is altered in various ways:

**Crossover children** Two or more individuals are combined to form a new one by mixing the solution's genome (here, the parameter vectors) in a randomised fashion.

**Mutation children** One or more parameters of the individual are altered randomly

**Elite children** have the best fitness level (lowest cost function) in the current generation and therefore remain unchanged

Additionally other steps may be added like eliminating individuals with a large cost function and creating new ones. Beside the mentioned basic approach, highly sophisticated methods have been developed to improve the optimisation process, for example, to prevent the population to gather around only one local optimum. The algorithm is stopped when the maximum number of generations is reached or the change in the fitness functions drops below a predefined tolerance value and a (local) minimum is found.

### 4.1.3 Methodology – Implementation of the Parameter Estimation

The genetic algorithm was chosen because of the time needed to evaluate the derivation of the cost function and the possibility of several local optima in the problem space. For the parameter estimation process the MATLAB built-in genetic algorithm was used in a constrained multi-objective setup (fit on the cross bar's position and the contact force). Constraints were put on each of the parameters to confine them to "reasonable" ranges (e.g. neither negative nor unrealistically large masses). Because of the large dimension of the estimation problem (more than 10 degrees of freedom), the genetic algorithm was used with a large population size of 1000 individuals. For each individual in every generation the following steps were done:

1. The equilibrium position of the nonlinear equations of motion for the given parameter set (including the measured steady state pressure  $p_0$  and the measured steady state force  $F_0$  are found by using the *fsolve* command in MATLAB, which itself is using the Levenberg-Marquardt algorithm. The result is the equilibrium position:  $\mathbf{x}_0$  (e. g.  $[\delta_0, \xi_0, \eta_0]^T$ ).
2. The linearisation of the nonlinear equations of motion is then done around the aforementioned point  $\mathbf{x}_0$ . For the linearisation *m*-files were created using Maple, so no numerical approximations of the derivatives had to be computed.

3. Use the input data of the measurement run to simulate the linear model
4. Calculate the fit of the linear model to the measurement data:

$$\text{fit}(\%) = 100 \cdot \left( 1 - \frac{\|\mathbf{y} - \hat{\mathbf{y}}\|}{\|\mathbf{y} - \text{mean}(\mathbf{y})\|} \right)$$

and return these values when the objective function is evaluated in the process of optimisation. The sequence  $\mathbf{y}$  denotes the measured data while  $\hat{\mathbf{y}}$  is the model's output.

The iterations were stopped when the maximum number of generations was reached or the average Pareto spread was too low (all individuals converged towards one point). To monitor the status of the time-demanding optimisation process after each finished generation, a Pareto front is displayed. This plot shows the dominating individuals of the population in the two optimisation criteria. An individual is Pareto-optimal if a decrease in one objective function is only possible if the other one increases. The solution of the optimisation process is a set approximating the Pareto front of quasi-Pareto-optimal solutions from which the user has to choose an appropriate one. The main advantage of this kind of result representation is that it is not necessary to tune weighting parameters a priori to make different measures or units comparable. Instead, the genetic algorithm tries to minimise both objective functions. An example of such Pareto front approximation is depicted in Figure 4.7.

## 4.2 Measurement Data

Since no information of the occurring frequencies (and their contribution to the overall dynamics) at the test bed was available, a rather high sampling frequency was chosen initially to make sure to capture all relevant physical effects well beyond the Nyquist frequency, which is half the sampling frequency. To verify that there are no aliasing effects in the measurements, two data acquisition runs with different sampling frequencies that are mutually prime were made. If relevant contributions in the frequency domain differ in both runs, either (analog) low-pass anti-aliasing filters have to be applied or the sampling frequency has to be increased. As Figure 4.1 shows this is not necessary due to the good agreement of the spectrograms of both measurement runs. Both signals show the force measurement with a constant valve input to the pneumatic actuator, while the linear motor follows a sine wave at 1 Hz. Remarkable are the surprisingly high frequency contents of the signals that are assumed to be caused by resonance behaviour of the testbed arrangement (a robot with a rather large overhang). Additionally, it later turned out that oscillations in the force signal are introduced by the placement of the force sensor between the slider of the linear motor and an aluminum bar.

The sampling frequency was then chosen to be 500 Hz and as a first step the recorded data were examined. The relevant signals were plotted separately and checked for outliers, as well as trends and non-stationarities [38]. Then the data recorded by the MicroAutoBox were resampled to 50 Hz, so that they had the same time basis as data

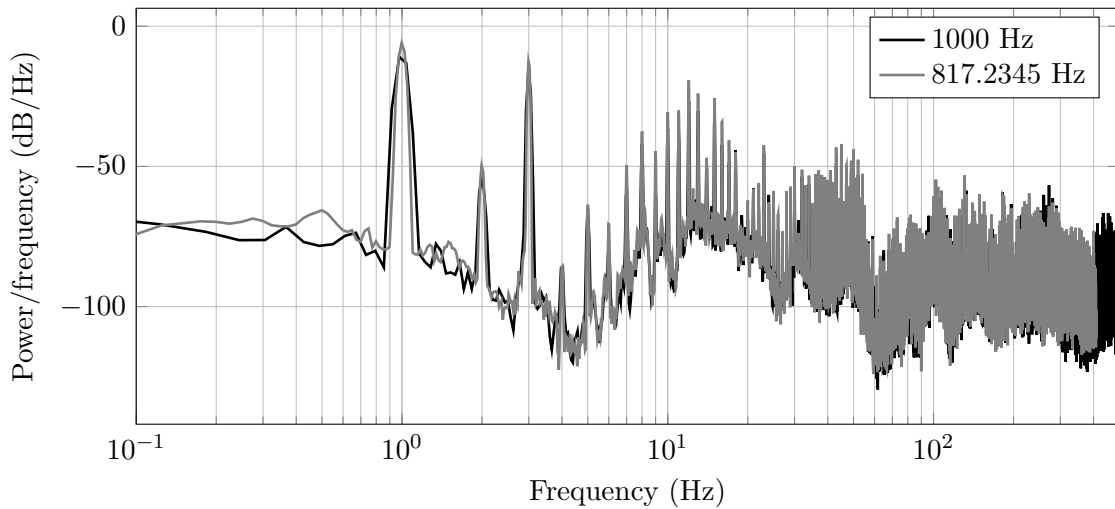


Figure 4.1: Spectrum of the force signal with two different sampling frequencies when the linear motor is excited with a 1 Hz sine.

extracted from the video recordings. Then, all data sets were low-pass filtered with a stop-band frequency of 20 Hz to focus on the relevant dynamics and also reduce the effect of measurement noise, as the Nyquist frequency of the video recordings is only 25 Hz. However, when the dynamics of the coupled system of the pantograph and catenary is under investigation, [39] suggest the frequencies beyond 30 Hz may be relevant as well.

The data sequence for the estimation process was either taken from a run with APRBS input signals (for both, the pressure and the linear motor position), or a combination of APRBS and ramp signals. Examples of both signals can be found in Figures 4.2 and 4.3. There, the influences of the inputs on the outputs can already be seen. Especially in the first figure, the force (although already filtered with a cut-off frequency of 20 Hz) appears very noisy or at least heavily oscillating with very high amplitudes. This is no original pantograph behaviour, but was artificially introduced by the force sensor in combination with the aluminium rack. As can be seen for example in Figure 3.9 on page 26 at the end of the linear motor's slider the force sensor is attached, followed by the aluminium beam with a weight of about 1.5 kg that eventually is in contact with the pantograph. This installation leads to the monitoring of the inertia force of the aluminium bar and therefore introduces unwanted dynamic contributions in the force measurement signal when the system is excited. A validation for that statement can be found in Figure 4.3, where both inputs (displacement and pressure) are ramp sequences with different durations. After the linear motor is at rest (after 60s) a smooth force signal can be observed. Prior to that, even though the velocities and accelerations are small, additional contributions to the force signal can be seen. Additionally, some tests with a mounted acceleration sensor were made which confirmed the interpretation.

In the following sections the results of the estimation process of the different models described in Chapter 2 are discussed. Before that, on the basis of the camera record-



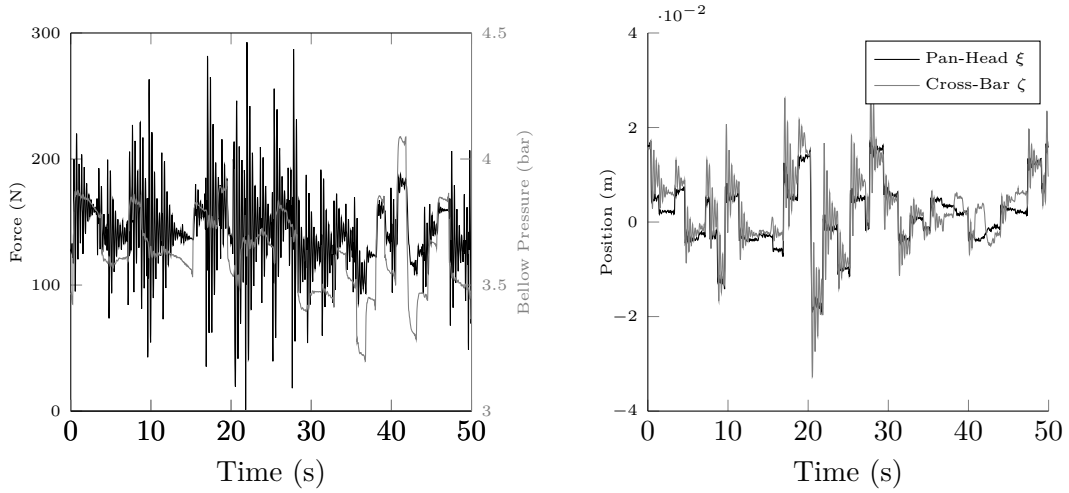


Figure 4.2: Recorded values for two distinct APRBS input sequences (linear motor's position and pressure)

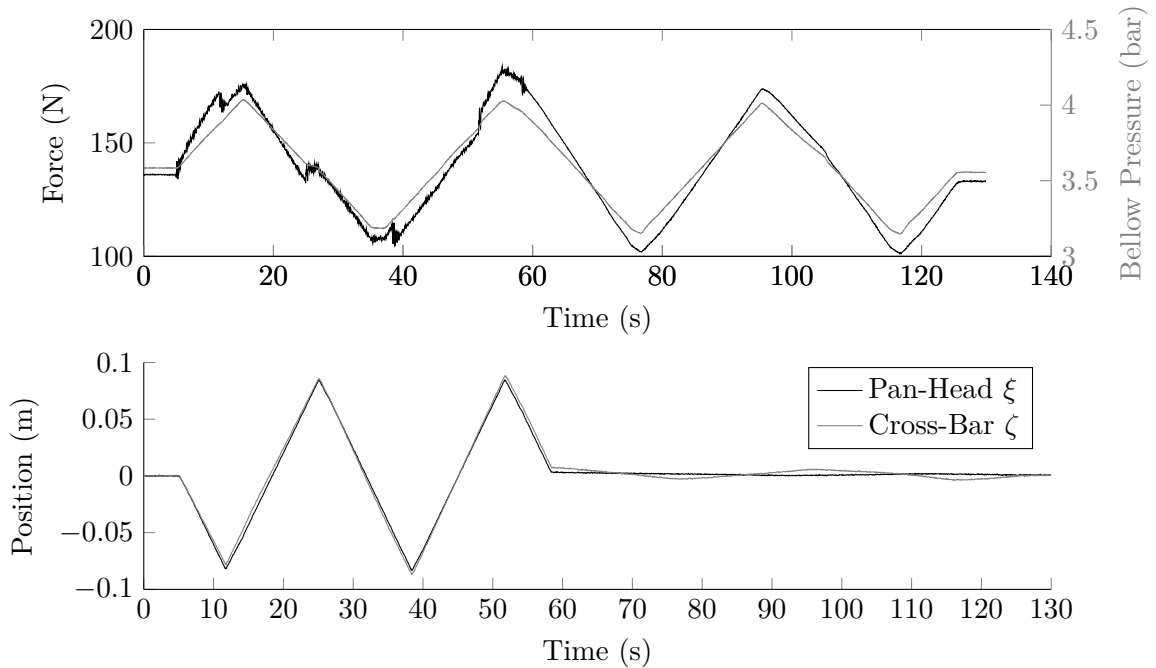


Figure 4.3: Recorded values for two distinct ramp input sequences (linear motor's position and pressure). During the first 60s the linear motor is moving and although already low-pass filtered, the oscillations of the force signal are clearly visible.

ings and the force signal, the pan head is analysed in more detail and a transfer function is estimated from the available data.

### 4.3 Collector-Head

The collector-head plays an important role in the pantograph dynamics since it is responsible for maintaining the contact in a high dynamics movement and has to quickly react to small disturbances. To ensure sufficient contact quality, regulations require a velocity-dependent mean contact force. At higher speeds, a loss of contact is even worse and so the contact force is increased at higher velocities. The two main strategies to increase the pantograph contact force are either to increase the bellow pressure with increasing velocities, which at least needs basic feed-forward control functionality, or to mount spoilers on the pantograph that lift the pantograph upwards with higher wind speeds.

The collector-head of the pantograph under test consists of four torsional springs that are located inside two tubes mounted on the cross bar as can be seen in Figure 2.1 on page 6. The design choice of placing the tubes under the cross bar with the center of rotation of the hinge directly above the cross bar leads to advantageous properties, especially in high-speed operation. Although the four suspensions springs of the two pan-heads are nominally independent of each other, a significant coupling could be observed when only one of them is actuated.

As a first test to examine the collector-head dynamics the transfer function between the cross bar and the pan-heads positions was estimated using a PT2 element. The result is shown in Figure 4.4. Because the position data was extracted from video recordings at 50 Hz, only information up to half of this frequency is available. However, because of the conversion process described in Chapter 3.3 the measurements are only reliable for frequencies up to 10 Hz. Below that, the transfer function from the position of the cross bar to the pan-head's position can very well be described by a PT2 element and the resonance frequency lies at 3 Hz. A high resonant peak at that frequency was also observed for the force measurement during a 1 Hz sine motion of the linear motor, shown in Figure 4.1. This indicates that significant nonlinearities are present.

When comparing only the two position signals of the cross-bar and the pan-heads, it is very likely that dynamics of the robot, the aluminium beam (the contact-wire imitation), or the arrangement of rods are mapped into one or both position measurements. To get a more accurate description of the collector-head's behaviour, a more thorough system analysis is made based on the model depicted in Figure 2.5 and the corresponding transfer function is formulated. It takes the force  $F_1$  acting on the pan-heads by the contact wire into account:

$$Y_{cb}(s) - Y_h(s) = \Delta Y(s) = \frac{\frac{1}{m}}{s^2 + \frac{c}{m}s + \frac{k}{m}} F_1(s) + \frac{s^2}{s^2 + \frac{c}{m}s + \frac{k}{m}} Y_2(s). \quad (4.15)$$

The resulting transfer functions are visualised in Figure 4.5 and can be used to identify the model parameters: mass, damping, and stiffness of the collector-head

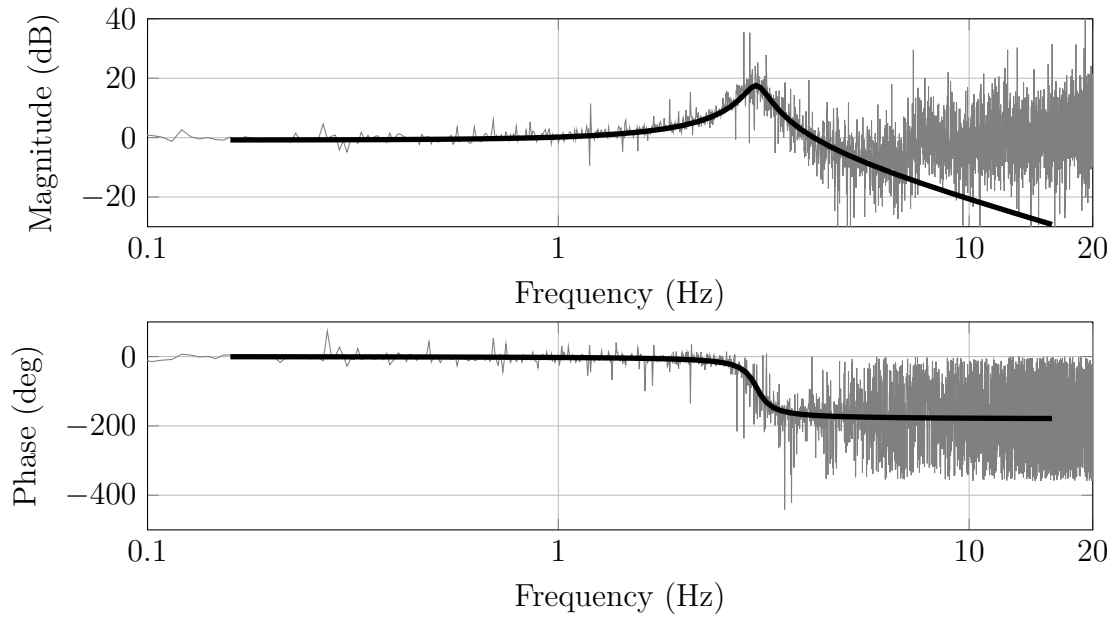


Figure 4.4: Measured position (gray) and estimated (black) transfer function from the cross-bars position to the pan-heads position.

when modelling it as a one-degree-of-freedom system.

When the influence of the cross bar position is neglected and only the transfer function from the force to the difference of the two positions is analysed, the fit is much better, as can be seen in Figure 4.6:

$$Y_{cb}(s) - Y_h(s) = \Delta Y(s) = \frac{\frac{1}{m}}{s^2 + \frac{c}{m}s + \frac{k}{m}} F_1(s). \quad (4.16)$$

The identified parameters of the PT2-elements depicted in Figure 4.5 and 4.6 are shown in the table below.

Parameter	Model (4.15)	Model (4.16)
m (kg)	9.7	13.3
c (N s/m)	97.2	24.1
k (N/m)	9589.5	13142.0

As will be shown in the next section, when the parameters of the whole pantograph's model are identified, the values of these parameters do vary, but still stay within a comparable range.

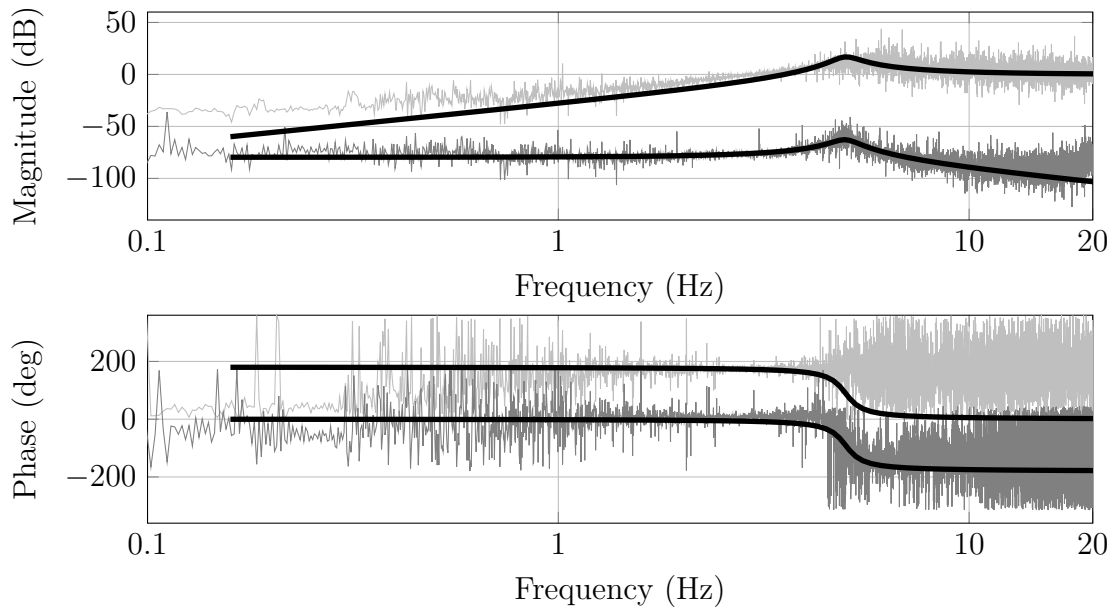


Figure 4.5: Measured (gray) and estimated (black) transfer functions from the cross-bars position and the force to the pan-heads relative position.

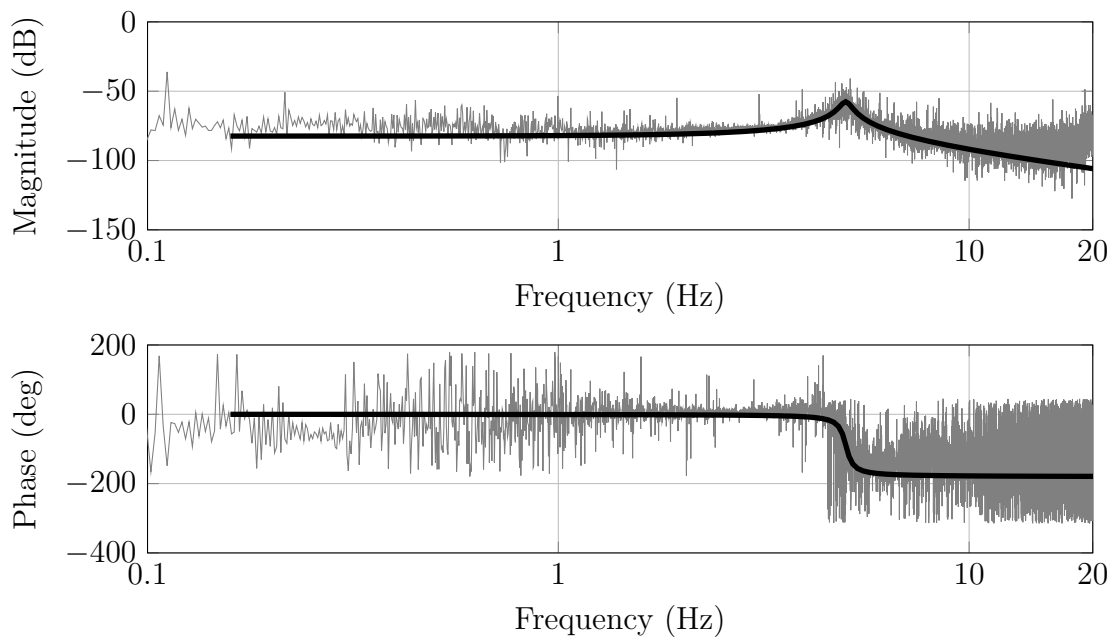


Figure 4.6: Measured (gray) and estimated (black) transfer functions from the force  $F_1$  to  $\Delta Y = y_{cb} - y_h$ .

## 4.4 Nonlinear Pantograph Model with Force Excitation

The first nonlinear gray-box pantograph model used considered a torque acting at the bottom and a vertical contact force at the pan-heads as inputs and is depicted in Figure 2.6 on page 11. Since the identification process using the whole nonlinear model was too time-consuming to be used, the nonlinear equations of motion were linearised around their equilibrium position for every set of parameters obtained during the run of the genetic algorithm. This way, the nonlinear equations of motion had to be processed only once, namely at the start of the simulation to obtain  $\mathbf{x}_0$  and not in every time step of the simulation of the differential equation.

However, the model turned out to be unstable around its equilibrium position, as a constant input moment leads to an unbounded rise or lowering of the pantograph. This was the case for both the nonlinear as well as the linearised equations of motion. Ad-hoc attempts to obtain a useful model have been tried, such as overriding the position of the pan-heads during the simulation with the measured values. However, this was not successful, so a different model structure, outlined in Section 4.5, had to be used.

## 4.5 Nonlinear Pantograph Model with Displacement Excitation

This model was already introduced in Section 2.5 and is depicted in Figure 2.8 on page 14. It eliminates the drawbacks of the previous nonlinear model. The agreement of the model output with the measurements is also good, and the Pareto front of the identification process according to Section 4.1 is shown in Figure 4.7.

The two axes show the estimation error (fit in %) of the cross-bar position and the contact force. Every marker in the plot represents one parameter set (also called ‘individual’ in the genetic algorithm) and each is approximately Pareto-efficient in the sense that a benefit in one direction leads to deterioration of the other cost function. The optimisation was carried out with a total of 13 parameters and an exemplary solution is shown in Table 4.1.

masses	kg	damping	N s/m	stiffness	N/m
$m_1$	22.1	$c_1$	277.7	$k$	1399423
$m_2$	4.5	$c_2$	329.4	$k_c$	21073
$m_3$	6.7	$c_3$	1082.8	$k_{ph}$	11931
$m_4$	21.1	$c_c$	65.8		
$m_c$	6.0				

Table 4.1: Selected solution of the estimation process

The remaining parameter was the factor to obtain the input moment given the bellow pressure and was estimated with 260.0 N m/bar. The masses  $m_1$  to  $m_4$  correspond to

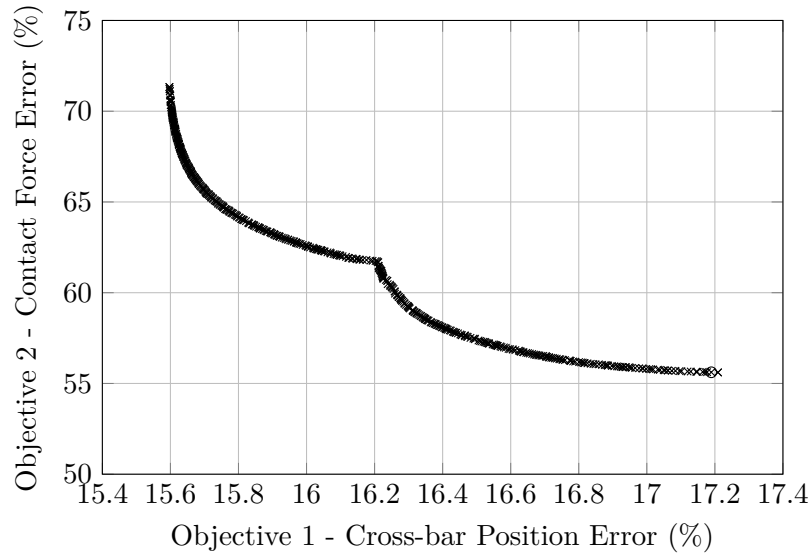


Figure 4.7: Pareto front of the identification process to the nonlinear pantograph model

the masses of each rod defined in Figure 2.8,  $c_1$  is the damping of  $\dot{\varphi}_1$ ,  $c_2$  that of  $\dot{\delta}$  and  $c_3$  that of  $\dot{\varphi}_2$ . The parameter  $k$  denotes the stiffness of the third rod and  $k_{ph}$  is the stiffness of the carbon pan-heads. All values with the subscript  $c$  are the parameters of the collector-heads.

The estimation process was done with the measurement data depicted in Figure 4.2 which consisted of uncorrelated step signals for the linear motor's position and for the desired bellow pressure. To validate the obtained model, it was tested with the input signals that were used for obtaining the data in Figure 4.3 and the result of the validation process is shown in Figure 4.8. The force signal from the nonlinear model (light gray) already follows the measurement signal (black) well, but some of the oscillations are exaggerated. The linearised version of the nonlinear model (dark gray) shows an even better behaviour. This is most probably due to the fact that the parameter estimation was done using a linearised version of the equations of motion using the current parameter set. Finally it should be mentioned that the oscillations were even worse when the input signal was more dynamic (like steps).

While remaining stable and being in good agreement with the measured data, this model also has a drawback. Since one of its inputs is a displacement and the spring representing the carbon contacts is stiff, the pantograph closely follows the motion of the contact wire. Theoretically, it would therefore be possible that the modelled pantograph is pulled upwards by the contact wire if the bellow pressure is too low to push the pantograph upwards. One way to circumvent this behaviour is to force the stiffness of the carbon contacts to a lower value, either by imposing constraints in the optimisation process or by setting it to a fixed value.

In the next test, the carbon contact stiffness is set to 50 000 N/m as given in the norm EN 50318 [27]. This led to a small change in the estimated parameters although they stayed in a comparable range. Typically, less than 10 % change in the parameter

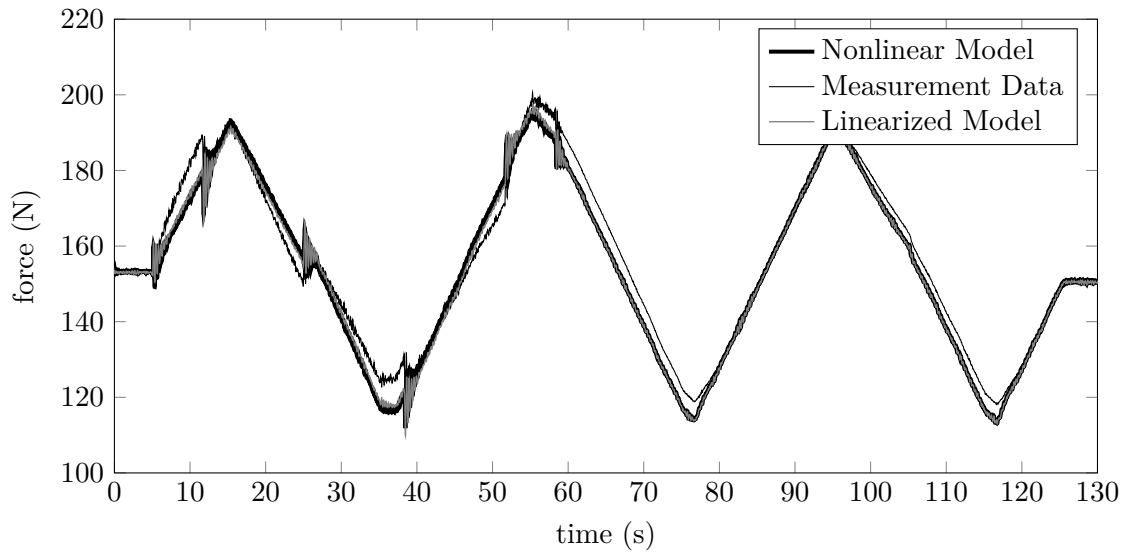


Figure 4.8: Force signal from the validation runs

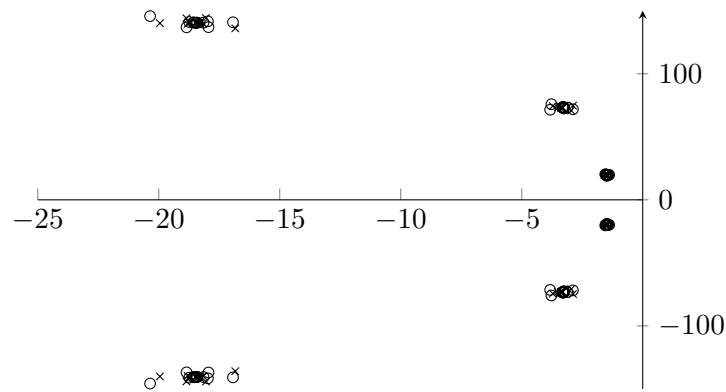


Figure 4.9: Eigenvalues of the linearised system when each of the parameters is multiplied by 0.9 (circles) and 1.1 (crosses), respectively

values occurred. The largest difference was at the stiffness of the carbon contact that increased from 10 458 N/m to 50 000 N/m. Both fits (cross-bar position and contact force) decreased but stayed in a plausible range too. The fit on the force calculated to 30.1 % on the training data and 82.4 % on the validation data.

Changing the problem to a single-objective optimisation problem and only minimising the force error led only to a very small improvement.

Figure 4.9 shows the eigenvalues of the linearised model when each parameter is sequentially multiplied by 0.9 (black) and 1.1 (gray), respectively. The position of the eigenvalues is rather robust to changes in the parameters and the overall dynamics is not significantly influenced by the parameter variation. A variation of the mass  $m_c$  of the collector-head as well as the stiffness  $k_{ph}$  of the topmost spring have the strongest influence on the model dynamics.

All results presented in this section were obtained by using the linearised version of

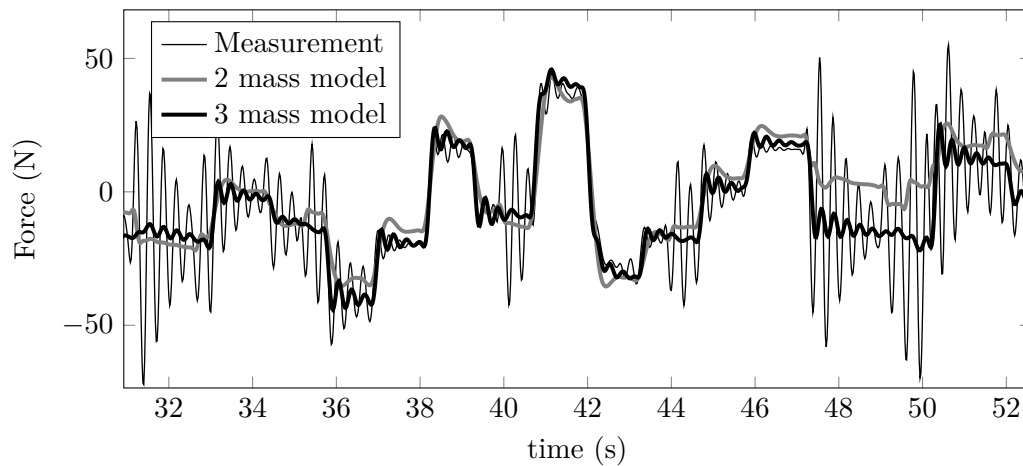


Figure 4.10: Force signal measured (black, thin) and the model output of the harmonic oscillators: 2-mass-model: gray, 3-mass-model: black, thick

the nonlinear equations of motion because computation times for the fully nonlinear model are too long to enable an optimisation on the whole nonlinear system.

## 4.6 Harmonic Oscillators

The linear three and two degrees of freedom models are often used in the literature and consist of three respectively two masses with springs and dampers between the masses and the inertial system. The input to the model could be either a force or a displacement if an additional spring is placed on the top mass, as was done here. A visualisation as well as the equation of motion were already given in Section 2.6 on page 14. The parameters of these models have only very limited physical meaning on the real pantograph but it is easily usable in simulations and parameter estimation because of its linearity. The parameter estimation process was done with the step sequence from Figure 4.3 and is computed quickly because no treatment of the nonlinear equations of motion of the pantograph is necessary. The input from the pneumatic actuator was modelled as a force acting on the first mass. Again, the force was assumed to be proportional to the pressure inside the bellow. The factor mapping pressure to force was modelled as an additional degree of freedom in the estimation process. The output of the models obtained is depicted in Figure 4.10, where a part of the force sequence is plotted. The three-mass oscillator gives significantly better results than the two-degree-of-freedom model.

## 4.7 Harmonic Oscillators with Friction

In this model the two-mass and three-mass structure from the previous section is taken but extended with two nonlinear Coulomb friction terms, already described



in Section 2.6 and 2.7 on page 14. This step is justified by the visible stick-slip effect when the height of the pantograph is slowly changed. Additionally, as already discussed, the pneumatic actuator's valve itself often exhibits such effect as well.

The performance increase with having friction terms in addition to the damping  $c_1$  and  $c_2$  for the two-mass structure only gave a slightly better fit on the force signal, however, the result on the validation data was much better than when using the linear two-mass oscillator. On the other hand, the linear three-mass oscillator has only one more parameter and fits much better even without an additional friction model.

If friction is added to the three-mass structure the fit on the training data surprisingly decreases to 13.0 %. One explanation is that a different parameter estimation algorithm has been utilised due to the nonlinear system model. However, the fit on the validation data is far better with 83.7 % which may be an indication that there is indeed significant Coloumb friction present in the pantograph, which becomes evident in slow, large scale motion sequences.

## 4.8 Summary

In this chapter the parameters of different model structures have been estimated and validated on measurement data. In principle, two different excitations are possible: force and position excitation. The problem becomes ill-posed when the force is taken as an input in combination with the chosen pneumatic actuator model in the sense that a rigid body mode is introduced that renders the system unstable. Hence, the position input was considered here. However, the derived models can be changed to the force input form by removing the contact spring and adding an input force instead.

Additionally, state space black box models with a dimension of 4 and 6 were estimated. The following table lists the results of model structures under investigation:

Model Structure	DOF	Fit APRBS (%)	Fit ramps (%)
Physical Model (linearised)	13	44.7	84.0
Black Box (6 states)	36	35.9	69
Black Box (4 states)	16	45.8	63.1
3-mass-oscillator w. friction	14	13.0	83.7
3-mass-oscillator	11	15.1	76.8
2-mass-oscillator w. friction	10	11.4	21.1
2-mass-oscillator	8	10.6	-76

In the third column the fit on the training data (the ARBS signal from Figure 4.3) is shown and in the fourth column the same parameter set was used on the validation data from Figure 4.2. The following observations can be made:

- The physical gray-box model (with 13 free variables) and a state space dimension of 6 performs very well on both data sets and its states are interpretable

in terms of physical meanings.

- The six-state black-box model with a total of 36 free variables performs worse than the four-state black-box model on the training data (probably due to convergence to a local optimum). However, on the validation data the more complex model outperforms the simpler one.
- The computational time needed to identify the parameters of the grey-box models is several hours, while the parameters for the black box models were obtained in several seconds. These times were taken on a modern office PC (Intel i7).
- The poor performance of the harmonic oscillator on the training data is due to the spurious oscillations in the force signal that are not fitted at all.
- The two-mass-oscillator fails completely on the validation data, while the three-mass-oscillator gives very good results.
- Considering friction slightly improves the result, but adds two (or three) unknown parameters. Additionally the advantages of having a linear model are lost.

# Chapter 5

## Design of Experiment — DoE

### 5.1 Introduction

The foregoing chapter dealt with extracting a model from already available measurement data after the test runs were completed. The topic *Design of Experiment (DoE)*, however, deals with the problem of how to obtain the maximum amount of information out of an upcoming or even ongoing experiment. The output of this process can be, for example, the optimal sampling time, the optimal sensor and actuator locations, or the optimal input signals. If more than one objective is under consideration, a joint design problem is necessary because these objectives are often interrelated [40]. Since there are always constraints in practical situations such as limited actuators, finite measurement time and maximum sampling rate, these have to be incorporated in the design of experiment task as well.

If it is possible to run the design process during an active experiment to, for example, obtain the next input value(s) depending on the current estimated model parameters, this is called online DoE. The advantage is that in every iteration step the actual optimal input is applied to the system depending on the newest parameter vector. So, on-the-fly, the inputs can be chosen in a way that the current variances of the parameter estimates are minimised.

### 5.2 Theory

The core of the DoE is the quantification of the (novel) information content of the given experiment. One suitable quantity for this purpose is the variance of the estimated variables: a smaller variance means high certainty of the parameter. A lower bound for the parameter covariance, which is reached by an efficient estimator, is the “Cramer-Rao” lower bound:

$$\text{cov } \hat{\boldsymbol{\theta}} = M^{-1}, \quad (5.1)$$

where  $M$  is the *Fisher information matrix*:

$$M = E_{y|\boldsymbol{\theta}} \left\{ \left( \frac{\partial \log p(y|\boldsymbol{\theta})}{\partial \boldsymbol{\theta}} \right) \left( \frac{\partial \log p(y|\boldsymbol{\theta})}{\partial \boldsymbol{\theta}} \right)^T \right\}. \quad (5.2)$$

Again,  $\boldsymbol{\theta}$  denotes the parameter vector,  $y$  the model output (respectively the vector of all measurements starting at zero time) and  $p$  is the probability density function of the sample. From the Cramer-Rao lower bound follows that a value related to  $M$  is a good representation of the information content of the experiment. Assuming an efficient estimator which reaches this bound, by maximising the Fisher information matrix the accuracy of the parameter estimation is increased. Introducing a scalar function  $\phi$ , a cost function  $J$  is to be minimised:

$$J = \mathbb{E}_{\boldsymbol{\theta}} [\phi(M)] \quad (5.3)$$

In the literature different functions operating on the Fisher information matrix exist, from which the most important ones are:

**A-Optimality** Here, the trace of the inverse of the Fisher matrix is minimised, which results in minimising the average variance of the estimated variables

**D-Optimality** Here, the determinant of the Fisher information matrix is maximised.

**E-Optimality** This criterion maximises the smallest eigenvalue of the Fisher information matrix.

The shape of Equation (5.2) is rather unsuitable for practical use since it involves an expectation over a matrix containing the product of two probability density functions. Assuming additive noise  $\varepsilon$  that is independent and Gaussian distributed with  $\mathcal{N}(0, \sigma^2)$  and that the chosen model structure represents the system's behaviour, the measured output can be written as the sum of the model's output and noise:

$$y(t) = y_m(t, \hat{\boldsymbol{\theta}}) + \varepsilon(t). \quad (5.4)$$

the noise then takes the following probability density function, from which the log likelihood can be computed:

$$p(y|\boldsymbol{\theta}) = \frac{1}{\sqrt{2\pi}\sigma^2} \exp^{-\frac{(y(t)-y_m(t,\hat{\boldsymbol{\theta}}))^2}{2\sigma^2}},$$

$$\log p(y|\boldsymbol{\theta}) = \underbrace{-\frac{N}{2} \log(2\pi\sigma^2)}_{\text{independent of } \boldsymbol{\theta}} - \sum_{k=1}^N \frac{((y(t_k) - y_m(t_k, \boldsymbol{\theta})))^2}{2\sigma^2},$$

where  $N$  different measurements (for example time steps in dynamical systems) are assumed and the partial derivation with respect to  $\boldsymbol{\theta}$  gives:

$$\frac{\partial \log p(y|\boldsymbol{\theta})}{\partial \boldsymbol{\theta}} = \sum_{k=1}^N \frac{y(t_k) - y_m(t_k, \boldsymbol{\theta})}{\sigma^2} \frac{\partial y_m(t_k, \boldsymbol{\theta})}{\partial \boldsymbol{\theta}}. \quad (5.5)$$

Plugging this result in the definition of the Fisher information matrix (5.2) and noting that all cross terms in the product of the sum vanish because of the expectation of the mutually independent noise:

$$\mathbb{E} \left[ \left( y(t_k) - y_m(t_k, \boldsymbol{\theta}) \right) \left( y(t_j) - y_m(t_j, \boldsymbol{\theta}) \right) \right] = \sigma^2 \delta_{kj},$$

where  $\delta_{ij}$  denotes the Kronecker delta function, a much more practical form of the Fisher information matrix is derived:

$$M(\boldsymbol{\theta}) = \sum_{k=1}^N \left\{ \frac{1}{\sigma^2} \frac{\partial y_m(t_k, \boldsymbol{\theta})}{\partial \boldsymbol{\theta}} \left( \frac{\partial y_m(t_k, \boldsymbol{\theta})}{\partial \boldsymbol{\theta}} \right)^T \right\}. \quad (5.6)$$

With this representation of the Fisher information matrix, the derivation of the model output has to be built with respect to each parameter and then divided by the noise variance. One can already see that by reducing the noise variance the information of the experiment is increased. Also, high values of the output's sensitivity on the parameters ( $\frac{\partial y_m}{\partial \boldsymbol{\theta}}$ ) increase the information content.

### 5.3 Example: Slope and Intercept of a Line

Assume that there is a line ( $y = f(x) = kx + d$ ) drawn and the task is to estimate the slope  $k$  and the intercept  $d$  with just two measurements. Let the line lie in the interval  $[-1, 1]$  and independent and identically distributed measurement noise  $\mathcal{N}(0, \sigma^2)$  is present because of reading errors and a coarse scale. The model consists of just two parameters:  $y = kx + d$  and  $N = 2$  (two measurements:  $y_1 = kx_1 + d$  and  $y_2 = kx_2 + d$ ). The partial derivative of the model output with respect to the parameters is:

$$\frac{\partial y_m(t_k, \boldsymbol{\theta})}{\partial \boldsymbol{\theta}} = [x_k \quad 1].$$

The Fisher information matrix according to Equation (5.6) then computes to:

$$M = \begin{pmatrix} \frac{x_1^2}{\sigma^2} + \frac{x_2^2}{\sigma^2} & \frac{x_1}{\sigma^2} + \frac{x_2}{\sigma^2} \\ \frac{x_1}{\sigma^2} + \frac{x_2}{\sigma^2} & \frac{1}{\sigma^2} + \frac{1}{\sigma^2} \end{pmatrix} = \frac{1}{\sigma^2} \begin{pmatrix} x_1^2 + x_2^2 & x_1 + x_2 \\ x_1 + x_2 & 2 \end{pmatrix}$$

Using the most common *D-Optimality* criterion the determinant of  $M$  has to be maximised:

$$\det(M) = \frac{(x_1 - x_2)^2}{\sigma^4}.$$

As expected, it is best to put the two measurement positions as far away as possible to maximise the information to be gathered and minimise the impact of measurement noise. Figure 5.1 visualises the result with placing the measurements (red dots) as far away from each other as possible.

Additional insight on the experiment can be obtained when the inverse of the information matrix is analysed, which is possible analytically with low effort for the case of two measurements. Equation (5.1) states that the inverse equals the covariance of the parameter estimation when an efficient estimator is used:

$$M^{-1} = \frac{\sigma^2}{(x_1 - x_2)^2} \begin{pmatrix} 2 & -(x_1 + x_2) \\ -(x_1 + x_2) & x_1^2 + x_2^2 \end{pmatrix}.$$

By choosing  $x_1 = -x_2$  it is possible to eliminate any covariance between the estimate of the slope and the intercept. This was automatically done by the optimisation

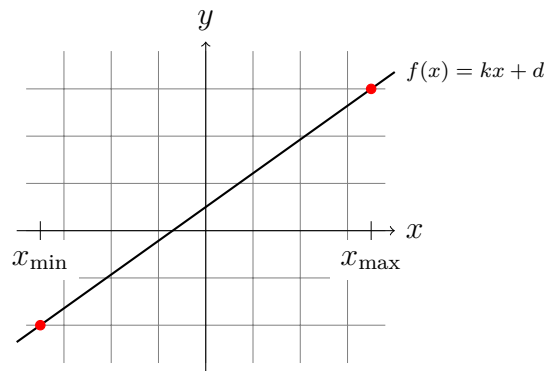


Figure 5.1: Result of the DoE for obtaining the slope and intercept of a line with two measurements (red dots).

problem because it also maximised the determinant of the Fisher matrix. In fact, for this simple example all of the optimality criteria listed in the beginning of this chapter lead to the same result. If three measurements are available, their position is not as intuitive any more. In fact, it is best to place the third measurement to either  $-1$  or  $+1$ , even though a non-zero covariance between the two parameters is then introduced. If this is not desired, the third measurement has to be set to  $x_3 = 0$ .

Although quite simple, this example gives the mathematical justification for the intuitive way of obtaining the two parameters of a line and also sketches the principal process of carrying out a design of experiment. Moreover, although theoretically only valid for efficient estimators, some information about the variance of the parameter estimation can be derived.

For problems that are linear in their parameters and thus can be formulated as  $\mathbf{y} = \mathbf{R}\boldsymbol{\theta} + \boldsymbol{\varepsilon}$ , it actually can be shown (see e.g. [41]) that the Fisher Information Matrix takes the following form:

$$M(\boldsymbol{\theta}) = \mathbf{R}^T \boldsymbol{\Sigma}^{-1} \mathbf{R},$$

where the diagonal matrix  $\boldsymbol{\Sigma}$  contains the noise variance of each measurement. Assuming the same noise process for each measurement, the equation can be simplified further and thus the originally cumbersome task of deriving the Fisher information matrix reduces to a matrix multiplication.

## 5.4 Example: Dynamical System

In the last section, a DoE for a static system is derived where the measurements were taken on arbitrarily chosen positions. In a causal dynamic system the measurements are in chronological order and are dependent on previous input values. Here, the oscillator depicted in Figure 5.2 is under investigation, where the force  $F$  is the input, the position  $y$  is the output and the three parameters  $m$ ,  $c$ ,  $k$  are to be estimated. Often actuators are limited in their dynamic performance or their amplitude is constrained. For example, the pneumatic actuator found at the bottom

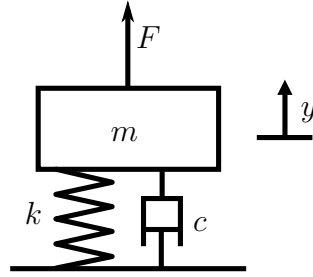


Figure 5.2: One degree of freedom oscillator

of the pantograph has a large time constant and thus only slowly reacts to pressure changes. Additionally, its operating range is limited in both directions. Therefore, input constraints are imposed in this example that limit the amplitude, as well as the rate of change of  $F(=u)$ :

$$|\Delta u| \leq \Delta u_{\max}, \quad (5.7)$$

$$|u| \leq u_{\max}. \quad (5.8)$$

The optimisation problem for maximising the determinant of the Fisher matrix (5.6) is thus formulated as:

$$\begin{aligned} & \underset{\Delta \mathbf{u}}{\text{maximise}} && \det(M(\Delta \mathbf{u})) \\ & \text{subject to} && |\Delta u_i| \leq \Delta u_{\max}, \quad i = 1, \dots, N, \\ & && \left| \sum_{k=1}^i \Delta u_k \right| \leq u_{\max}, \quad i = 1, \dots, N. \end{aligned} \quad (5.9)$$

The optimisation result is now the increment of the control input and not the control input itself. This way it is possible to consider constraints on the rate more easily. The optimisation problem can be brought into the linear inequality constraint notation of the form  $\mathbf{A}\Delta \mathbf{u} \leq \mathbf{b}$ .

At first, an offline DoE is designed and afterwards its results are compared to the output of an online DoE which incorporates a recursive least squares algorithm as well.

The continuous-time transfer function of the system shown in Figure 5.2 is easily obtained and reads as follows:

$$G(s) = \frac{\frac{1}{m}}{s^2 + \frac{c}{m}s + \frac{k}{m}}.$$

For the use in a digital system a discrete time version of the transfer function is obtained via a zero-order-hold element:

$$H(z) = (1 - z^{-1}) \mathcal{Z} \left\{ \mathcal{L}^{-1} \left( \frac{1}{s} G(s) \right) \right\}, \quad (5.10)$$

resulting in a discrete-time transfer function of the form:

$$H(z) = \frac{b_1 z^{-1} + b_2 z^{-2}}{1 + a_1 z^{-1} + a_2 z^{-2}}, \quad (5.11)$$

where the parameters  $\boldsymbol{\theta} = [a_1, a_2, b_1, b_2]$  are (strongly nonlinear) functions of  $m, c, k$ , as well as the sampling time  $T_s$ . The system equation for each time step  $k$  therefore is:

$$y(k) = \frac{b_1 z^{-1} + b_2 z^{-2}}{1 + a_1 z^{-1} + a_2 z^{-2}} u(k) + \varepsilon(k) = H(z)u(k) + \varepsilon(k) = y_m(k) + \varepsilon(k), \quad (5.12)$$

where  $\varepsilon$  denotes the measurement noise which is assumed i.i.d. and Gaussian with a known standard deviation  $\sigma$ .

The next step to obtain the Fisher information matrix is the derivation of the model output with respect to each parameter. The process is exemplified for the parameter  $a_2$ :

$$\begin{aligned} \frac{\partial y_m(k)}{\partial a_2} &= -\frac{b_1 z^{-1} + b_2 z^{-2}}{(1 + a_1 z^{-1} + a_2 z^{-2})^2} z^{-2} u(k) \\ &= -\frac{b_1 z^{-1} + b_2 z^{-2}}{1 + a_1 z^{-1} + a_2 z^{-2}} u(k) \frac{z^{-2}}{1 + a_1 z^{-1} + a_2 z^{-2}} \frac{b_1 z^{-1} + b_2 z^{-2}}{b_1 z^{-1} + b_2 z^{-2}} \frac{u(k)}{u(k)} \\ &= -\frac{\underbrace{b_1 z^{-1} + b_2 z^{-2}}_{y_m(k)} u(k)}{1 + a_1 z^{-1} + a_2 z^{-2}} \frac{z^{-2}}{1 + a_1 z^{-1} + a_2 z^{-2}} \frac{b_1 z^{-1} + b_2 z^{-2}}{b_1 z^{-1} + b_2 z^{-2}} \frac{u(k)}{u(k)} \\ &= -\frac{y_m(k-1)^2}{b_1 u(k-1) + b_2 u(k-2)} \end{aligned}$$

The process for the other derivations is similar and the whole sensitivity vector  $\mathbf{v}$  then reads:

$$\mathbf{v} = \frac{\partial y_m(k)}{\partial \boldsymbol{\theta}} = \begin{bmatrix} \frac{-y_m(k)y_m(k-1)}{b_1 u(k-1) + b_2 u(k-2)}, & \frac{-y_m(k-1)^2}{b_1 u(k-1) + b_2 u(k-2)}, \\ \frac{y_m(k-1)u(k)}{b_1 u(k-1) + b_2 u(k-2)}, & \frac{y_m(k-2)u(k)}{b_1 u(k-1) + b_2 u(k-2)} \end{bmatrix}^T. \quad (5.13)$$

The goal of optimal DoE is to find a sequence of input values  $u(1), u(2), \dots, u(N)$  that maximises the Fisher information matrix:

$$M(\boldsymbol{\theta}) = \frac{1}{\sigma^2} \sum_{k=1}^N \frac{\partial y(k)}{\partial \boldsymbol{\theta}} \left( \frac{\partial y_m(k)}{\partial \boldsymbol{\theta}} \right)^T. \quad (5.14)$$

For the DoE process a state vector is defined

$$\mathbf{x} = [x_1 \quad x_2 \quad x_3]^T = [y_m(k) \quad y_m(k-1) \quad y_m(k-2)]^T, \quad (5.15)$$

with which all the values in equation (5.13) can be calculated since the input values  $u(k)$  are known. The update equation is as follows:

$$\mathbf{x}(k+1) = [-a_1 x_1(k) - a_2 x_2(k) + b_1 u(k) + b_2 u(k-1), \quad x_1(k), \quad x_2(k)]^T. \quad (5.16)$$

The offline-DoE algorithm for obtaining an optimal input sequence is then as follows:



1. Calculate  $\boldsymbol{\theta} = [a_1, a_2, b_1, b_2]^T$  from the best possible guess for the parameters  $m, c, k$ .
2. Specify the sampling time  $T_s$ , as well as the end time from which the number of samples  $N$  can be calculated.
3. Start the optimisation algorithm (e.g. genetic algorithm), where in each iteration (and for each individual) the following steps are traversed in the objective function: Initialise the Fisher matrix  $M$  with a  $4 \times 4$  zero matrix and the state vector  $\mathbf{x}$  (5.15) with zero. Then repeat the following steps inside a loop  $N$ -times (until the end time is reached):
  - a) Update the state vector according to equation (5.16)
  - b) Calculate the parameter sensitivity vector  $\mathbf{v}$  according to (5.13)
  - c) Update the Fisher information matrix  $M$ :  $M = M + \mathbf{v}\mathbf{v}^T\sigma^{-2}$
 Then return the scalar cost function (5.3) (depending on the chosen optimality criterion) on  $M$  to the optimisation algorithm
4. The result of the optimisation is the optimal input sequence that should be applied to the system

For the online-DoE a few modifications to the above procedure have to be made: At every time step the genetic algorithm is started with a shorter horizon and the state vector is not initialised zero but with the past values. Then the first element of the obtained optimised input sequence is taken as the next input to the real system. Additionally, a recursive least squares algorithm is running in parallel to obtain a current guess for the model parameters  $\boldsymbol{\theta}$  from which the physical parameters  $m, c$  and  $k$  can be calculated by solving a system of nonlinear equations.

Both variants were tested in a simulation with the following setting:

$$[m, c, k]_{\text{real}}^T = [1 \text{ kg}, 2 \text{ N s/m}, 20 \text{ N/m}]^T, \quad (5.17)$$

$$[m, c, k]_{\text{init}}^T = [2 \text{ kg}, 10 \text{ N s/m}, 25 \text{ N/m}]^T, \quad (5.18)$$

$$T_s = 0.1 \text{ s} \quad (5.19)$$

$$T_{\text{end}} = 30 \text{ s} \quad (5.20)$$

$$\Delta u_{\text{max}} = 0.25 \text{ N} \quad (5.21)$$

$$u_{\text{max}} = 1.5 \text{ N} \quad (5.22)$$

$$\sigma^2 = 1 \times 10^{-10} \text{ m}^2, \quad (5.23)$$

The parameter vector  $\boldsymbol{\theta}$  consists of the four parameters  $[a_1, a_2, b_1, b_2]$ , see (5.11):

$$\boldsymbol{\theta}_{\text{real}} = [-1.6405, 0.8187, 0.0046, 0.0043]^T \quad (5.24)$$

$$\boldsymbol{\theta}_{\text{init}} = [-1.5092, 0.6065, 0.0021, 0.0018]^T. \quad (5.25)$$

Figure 5.3–5.5 each show the input sequence and the resulting output for the three test cases. At first, a superposition of two harmonic waves that does not violate

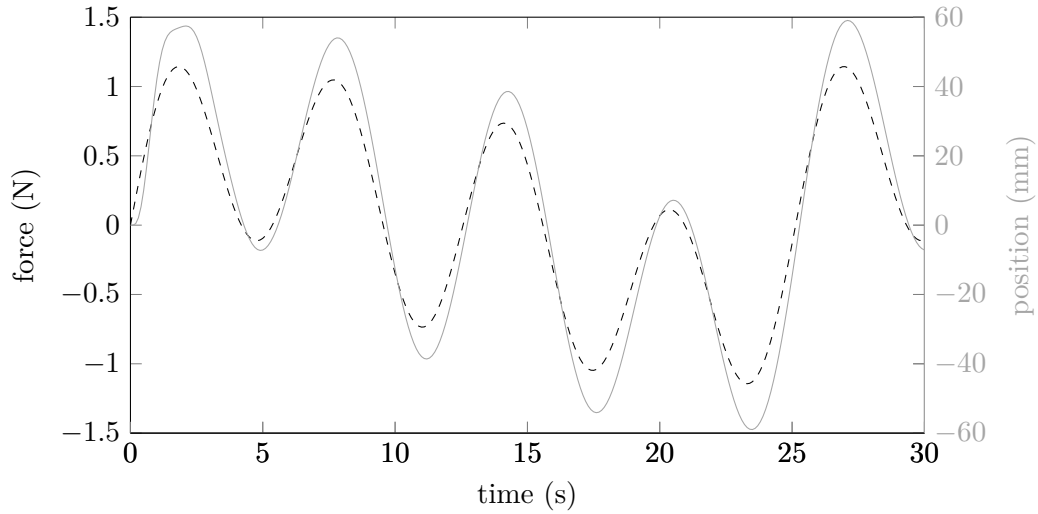


Figure 5.3: Input (force, dashed) and corresponding system response (position, gray) obtained with the sine wave force signal.

the input constraints is tested, denoted with *sine*. The input signal (dashed), as well as the resulting system output (solid) are visualised in Figure 5.3. This sine superposition was also used as the start input sequence for the *online*- and *offline* DoE optimisation. For the online DoE in each time step the parameter estimation is updated and therefore the DoE in each sample is started with the currently optimal parameter guess. To reduce the computation time the number of degrees of freedom for the optimisation problem is set to 20, i.e. only the next 20 input values are optimised.

The following parameter vectors  $\hat{\theta}$ , as well as the corresponding  $P$ -matrices from the recursive-least-squares algorithm (that are proportional to the covariance matrices) were obtained,

$$\hat{\theta}_{\text{sine}} = \begin{bmatrix} -1.5986 \\ 0.8049 \\ 0.0109 \\ -0.0011 \end{bmatrix}, \quad P_{\text{sine}} = \begin{pmatrix} 293.1 & -17.3 & -19.4 & 33.4 \\ -17.3 & 286.0 & -34.0 & 47.3 \\ -19.4 & -34.0 & 6.7 & -9.4 \\ 33.3 & 47.3 & -9.4 & 13.4 \end{pmatrix}, \quad (5.26)$$

$$\hat{\theta}_{\text{offline}} = \begin{bmatrix} -1.6233 \\ 0.8060 \\ 0.0056 \\ 0.0034 \end{bmatrix}, \quad P_{\text{offline}} = \begin{pmatrix} 27.00 & -19.64 & -0.44 & 0.92 \\ -19.64 & 17.59 & -0.15 & -0.06 \\ -0.44 & -0.15 & 0.15 & -0.17 \\ 0.92 & -0.06 & -0.17 & 0.22 \end{pmatrix}, \quad (5.27)$$

$$\hat{\theta}_{\text{online}} = \begin{bmatrix} -1.6372 \\ 0.8152 \\ 0.0027 \\ 0.0060 \end{bmatrix}, \quad P_{\text{online}} = \begin{pmatrix} 22.00 & -16.69 & -0.32 & 0.71 \\ -16.69 & 15.00 & -0.05 & -0.16 \\ -0.32 & -0.05 & 0.1 & -0.12 \\ 0.71 & -0.16 & -0.12 & 0.15 \end{pmatrix}, \quad (5.28)$$

where the positive influence of the DoE is clearly visible. The parameters were estimated more accurately and the covariances could be reduced by approximately

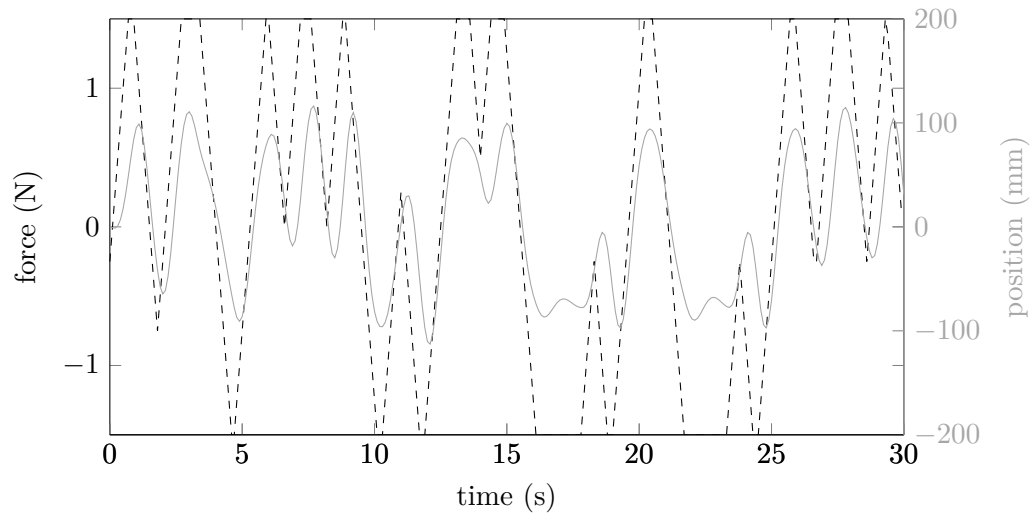


Figure 5.4: Input (force, dashed) and corresponding system response (position, gray) obtained with the force signal from the offline DoE.

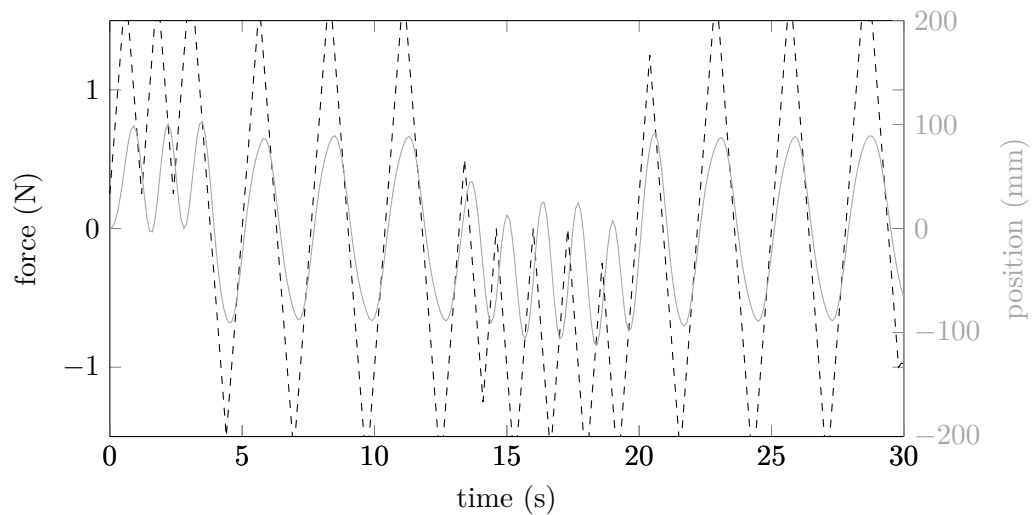


Figure 5.5: Input (force, dashed) and corresponding system response (position, gray) obtained with the force signal from the online DoE.

one magnitude. Since the shown  $P$ -Matrices are proportional to the covariance of the estimates (and thus inversely proportional to the Fisher information matrix in the case of an efficient estimator), one can clearly see that the parameters were estimated more accurately. Additionally, the online DoE was able to improve the result of the offline DoE because the starting guess for the parameters was not very close to the real values.

Additionally, with the obtained input/output data a time-domain parameter estimation process was started using the built-in MATLAB *greyest* command to identify the parameters of a gray-box model, which confirms the results from the recursive least squares procedure (see Table 5.1). The obtained input sequences show superior performance in the continuous-time estimation as well.

	real	init	sine	var	offline	var	online	var
$m$	1.0	2	0.90	0.087	0.90	0.018	0.91	0.019
$c$	2.0	10	1.81	0.118	1.71	0.043	1.85	0.049
$k$	20.0	25	20.14	0.123	20.08	0.187	20.05	0.25

Table 5.1: Result of the gray-box estimation in MATLAB. Shown are the estimated values as well as their variances (var).

## 5.5 Application to Pantograph Testbed

The principles of the Design of Experiments can be applied to pantograph test runs as well. To do so, the same approach as in the last example can be taken. One of the system structures described in Chapter 2 has to be chosen and its representation has to be transferred into a discrete-time transfer function. It is also possible to design an experiment whose goal is the discrimination between different model structures [42]. Then the next input point is set to maximise the difference between the output of both models, so the choice between the two (or more) structures is eased. Let us assume that just one model structure is selected and the parameters of the discrete-time transfer function are to be estimated with as much accuracy as possible. For the offline DoE the size of the parameter vector does not really matter since the whole sequence is computed before going to the test stand. In the online-DoE however, the numbers of parameter should be kept as small as possible in order to accelerate the optimisation process.

Additionally, there are significant constraints on the absolute input values as well as on the rate of change present on the pantograph testbed. The linear motor — though capable of high dynamic movements — is not able to closely follow step inputs. Much more limiting is the slow dynamic response of the pneumatic actuator that needs to be taken into account in the design of experiment process.

Here, only discrete-time transfer functions were investigated because of the discrete nature of the underlying control unit. Moreover, the application of the pantograph model lies most likely in a discrete-time setup as well. If the parameters are estimated accurately in the  $Z$ -domain, the conversion to continuous time (physical) parameters

should be accurate too. Additionally, the discrete signal obtained from discrete-time DoE can be used in a continuous-time parameter estimation problem, as was demonstrated at the end of the last section. Moreover, the theory for discrete-time DoE is well established, but if a continuous-time approach is sought, the procedure is more cumbersome, see for example Ref. [43]. The input signal derived is then represented in its frequency components.

# Chapter 6

## Summary/Outlook

In this work a pantograph model based on physical principles was derived and its parameters were estimated. This was done with measurement data obtained from a full-size high-speed train pantograph current-collector in a test bed setup. Data acquisition and testbed interface development were also part of this work. To obtain more information from the different parts of the pantograph, coloured labels were attached to the unit under test, and their position information was retrieved afterwards from recordings made with a video camera. The available information was then used to obtain the parameters of the gray-box-model and validated against other measurement data. The derived model structure was compared to other models found in the literature, such as a two- or three-mass-oscillator. Finally, a black-box-model was derived to evaluate and compare structured versus generic modelling approaches.

The derived pantograph model is capable of exactly reproducing the kinematics of the real pantograph. The apparent flexibilities of the system were modelled into one artificial state that describes the length variation of one of the rods. The collector head dynamics are sufficiently well approximated by a one-mass oscillator, and the resulting full pantograph model has six degrees of freedom. Because of the unknown relationship between the bellow pressure and the applied torque it was assumed that there exists a linear connection between these two quantities. With the help of a future pneumatic actuator test bed, the torque that lifts the pantograph upwards can be modelled more accurately. Because of this torque input at the bottom, a force excitation at the pan-heads leads to an unstable system and thus the position of the catenary was defined as the other input to the model. Alternatively, with the developed modelling framework the model structure can be easily altered to, for example, an angle-dependent uplift force (spring) and a force excitation by the catenary.

The testbed connection was successfully realised via a real-time dSPACE platform, and a flexible user interface was developed. Different excitation signals can be deployed on the linear motor (setting the emulated catenary's position) and the bellow. The same dSPACE platform is also responsible for data acquisition. Additionally, video recordings from the test runs were made and position information of different pantograph parts were extracted. The measurements were available at different sampling rates and had to be synchronised accurately. To do so, a synchronization

sequence was captured by both measurement systems.

Afterwards, parameters of different model structures were estimated and the output of the obtained models were compared. Although the testbed setup was ill-conditioned due to an oscillating mass between the pantograph and the force sensor, as well as a not perfectly rigid robot that both introduced unwanted oscillations in the force measurement signal, the derived model could describe the system dynamics well and was superior to the other models.

In the last chapter a method called *design of experiment* (DoE) was described and its application demonstrated on two examples that enables one to retrieve the maximum information out of an experiment by optimising the input sequence for future test runs. Since one of the examples treated a dynamical system, the adoption to the pantograph case is straightforward.

Future work could for example consist of additional measurement runs because the testbed was modified recently, and the influence of the oscillating mass leading to a deteriorated force signal was greatly reduced. If a more accurate model of the pantograph is needed, more test runs with different operating conditions (height, pressure, force) can be done and a set of local linear model trees (LOLIMOT) can be derived. This leads to a numerically efficient system representation that is valid over a large operating range and expected to significantly shorten computation time.

# Bibliography

- [1] A Carnicero, JR Jiménez-Octavio, M Such, A Ramos, and C Sánchez-Rebollo. Influence of static and dynamics on high performance catenary designs. In *Pantograph Catenary Interaction Framework for Intelligent Control*. PACIFIC, 2011.
- [2] Simon Walters, Ahmed Rachid, and Augustin Mpanda. On modelling and control of pantograph catenary systems. In *International Conference on Pantograph Catenary Interaction Framework for Intelligent Control*, PACIFIC, 2011.
- [3] Benedetto Allotta, Luca Pugi, and Fabio Bartolini. Design and experimental results of an active suspension system for a high-speed pantograph. *Mechatronics, IEEE/ASME Transactions on*, 13(5):548–557, 2008.
- [4] A Collina, A Facchinetti, and F Resta. A feasibility study of an aerodynamic control for a high speed pantograph. In *Advanced intelligent mechatronics, 2007 IEEE/ASME international conference on*, pages 1–6. IEEE, 2007.
- [5] Giorgio Corriga, Alessandro Giua, Walter Matta, and Giampaolo Usai. Frequency-shaping design of a gain-scheduling controller for pantographs. In *Decision and Control, 1994., Proceedings of the 33rd IEEE Conference on*, volume 1, pages 393–398. IEEE, 1994.
- [6] G. Gilbert and H.E.H. Davies. Pantograph motion on a nearly uniform railway overhead line. *Proceedings of the Institution of Electrical Engineers*, 113(3):485–492, 1966.
- [7] JiR Ockendon and AB Tayler. The dynamics of a current collection system for an electric locomotive. *Proceedings of the Royal Society of London. A. Mathematical and Physical Sciences*, 322(1551):447–468, 1971.
- [8] George C Vesely. *Modelling and experimentation of pantograph dynamics*. PhD thesis, Massachusetts Institute of Technology, 1983.
- [9] Jong-Hwi Seo, Hiroyuki Sugiyama, and Ahmed A Shabana. Three-dimensional large deformation analysis of the multibody pantograph/catenary systems. *Non-linear Dynamics*, 42(2):199–215, 2005.



- [10] M Arnold and B Simeon. Pantograph and catenary dynamics: a benchmark problem and its numerical solution. *Applied Numerical Mathematics*, 34(4):345–362, 2000.
- [11] J Pombo and J Ambrosio. Influence of pantograph suspension characteristics on the contact quality with the catenary for high speed trains. *Computers & Structures*, 110:32–42, 2012.
- [12] Weihua Zhang, Yi Liu, and Guiming Mei. Evaluation of the coupled dynamical response of a pantograph—catenary system: contact force and stresses. *Vehicle System Dynamics*, 44(8):645–658, 2006.
- [13] Aldo Balestrino, Ottorino Bruno, Alberto Landi, and Luca Sani. Innovative solutions for overhead catenary-pantograph system: wire actuated control and observed contact force. *Vehicle System Dynamics*, 33(2):69–89, 2000.
- [14] Shahin Hedayati Kia, Fabio Bartolini, Augustin Mpanda-Mabwe, and Roger Ceschi. Pantograph-catenary interaction model comparison. In *IECON 2010-36th Annual Conference on IEEE Industrial Electronics Society*, pages 1584–1589. IEEE, 2010.
- [15] G. Poetsch, J. Evans, R. Meisinger, W. Kortüm, W. Baldauf, A. Veitl, and J. Wallaschek. Pantograph/catenary dynamics and control. *Vehicle System Dynamics*, 28(2-3):159–195, 1997.
- [16] Frederico Grases Rauter, João Pombo, Jorge Ambrósio, and Manuel Pereira. Multibody modeling of pantographs for pantograph-catenary interaction. In *IUTAM Symposium on Multiscale Problems in Multibody System Contacts*, pages 205–226. Springer, 2007.
- [17] J. Pombo, J. Ambrósio, M. Pereira, F. Rauter, A. Collina, and A. Facchinetti. Influence of the aerodynamic forces on the pantograph—catenary system for high-speed trains. *Vehicle System Dynamics*, 47(11):1327–1347, 2009.
- [18] Lars Drugge, Tobias Larsson, Ansel Berghuvud, and Annika Stensson. The nonlinear behaviour of a pantograph current collector suspension. *Proceedings of the 1999 ASME DETC, Las Vegas NV, September*, pages 12–15, 1999.
- [19] Lars Drugge, Tobias Larsson, and Annika Stensson. Modelling and simulation of catenary-pantograph interaction. *Vehicle System Dynamics*, 33:490–501, 1999.
- [20] A Collina, A Facchinetti, F Fossati, and F Resta. An application of active control to the collector of an high-speed pantograph: simulation and laboratory tests. In *Decision and Control, 2005 and 2005 European Control Conference. CDC-ECC'05. 44th IEEE Conference on*, pages 4602–4609. IEEE, 2005.
- [21] Aleksandrs Matvejevs and Andrejs Matvejevs. Pantograph-catenary system modeling using MATLAB-simulink algorithms. *Scientific Journal of Riga Technical University. Computer Sciences*, 42(1):38–44, 2010.

- [22] Frederico Grases Rauter, João Pombo, Jorge Ambrósio, Jérôme Chalansonnet, Adrien Bobillot, and Manuel Seabra Pereira. Contact model for the pantograph-catenary interaction. *Journal of System Design and Dynamics*, 1(3):447–457, 2007.
- [23] Heinz Parkus. *Mechanik der festen Körper*. Springer, 1966.
- [24] H. Goldstein. *Classical Mechanics*. Addison-Wesley Publishing Company, 1980.
- [25] K. Ogata. *Modern Control Engineering*. Instrumentation and controls series. Prentice Hall, 2010.
- [26] EN 50318. Railway applications. current collection systems. validation of simulation of the dynamic interaction between pantograph and overhead contact line. 2002.
- [27] JP Massat, JP Laine, and A Bobillot. Pantograph–catenary dynamics simulation. *Vehicle System Dynamics*, 44(supplement):551–559, 2006.
- [28] Jin-Sung Paik, Chan-Kyoung Park, Yong-Guk Kim, and Ki-Hwan Kim. A study on the measuring system of contact force of pantograph for the high-speed train. *Journal of Advanced Mechanical Design, Systems, and Manufacturing*, 6(1):140–148, 2012.
- [29] J Pombo and J Ambrósio. Environmental and track perturbations on multiple pantograph interaction with catenaries in high-speed trains. *Computers & Structures*, 124:88–101, 2013.
- [30] Ning Zhou and Weihua Zhang. Investigation on dynamic performance and parameter optimization design of pantograph and catenary system. *Finite Elements in Analysis and Design*, 47(3):288–295, 2011.
- [31] Christian Saliger. Konzipierung und Realisierung eines Erprobungsprüfstandes im Zuge der Entwicklung geregelter Dachstromabnehmer. Master’s thesis, FH Technikum Wien, 2013.
- [32] Michael Deflorian and Susanne Zaglauer. Design of experiments for nonlinear dynamic system identification. In *IFAC 18th World Congress, Milano 2011*, 2011.
- [33] Alexander Schirrer, Emir Talic, and Martin Kozek. A flexible matlab-based simulation framework for dynamic catenary-pantograph interaction and co-simulation. In *2013 8th EUROSIM Congress on Modelling and Simulation*, pages 288–293. IEEE, 2013.
- [34] Lennart Ljung. *System identification*. Wiley Online Library, 1999.
- [35] Kaj Madsen, Hans Bruun, and Ole Tingleff. Methods for non-linear least squares problems. 1999.

- 
- [36] Kenneth Levenberg. A method for the solution of certain problems in least squares. *Quarterly of applied mathematics*, 2:164–168, 1944.
- [37] Donald W Marquardt. An algorithm for least-squares estimation of nonlinear parameters. *Journal of the Society for Industrial & Applied Mathematics*, 11(2):431–441, 1963.
- [38] Lennart Andersson, Ulf Jönsson, Karl Henrik Johansson, and Johan Bengtsson. A manual for system identification. *Laboratory Exercises in System Identification. KF Sigma i Lund AB. Department of Automatic Control*.
- [39] Andrea Collina and Stefano Bruni. Numerical simulation of pantograph-overhead equipment interaction. *Vehicle System Dynamics*, 38(4):261–291, 2002.
- [40] G.C. Goodwin and R.L. Payne. *Dynamic System Identification: Experiment Design and Data Analysis*. Mathematics in science and engineering. Academic Press, 1977.
- [41] Eric Walter and Luc Pronzato. *identification of parametric models from experimental data*. Springer, 2010.
- [42] Luc Pronzato. Optimal experimental design and some related control problems. *Automatica*, 44(2):303–325, 2008.
- [43] P.H. Kirkegaard. *Optimal Design of Experiments for the Parametric Identification of Civil Engineering Structures*. PhD thesis, Aalborg University, Denmark, 1991.